nature cardiovascular research

Article

https://doi.org/10.1038/s44161-023-00325-8

Critical shifts in lipid metabolism promote megakaryocyte differentiation and proplatelet formation

Received: 8 February 2023

Accepted: 27 July 2023

Published online: 31 August 2023

Check for updates

Bianca de Jonckheere[1,2,10], Ferdinand Kollotzek[3,4,10], Patrick Münzer[3,4], Vanessa Göb[5,6], Melina Fischer[3,4], Kristina Mott[5], Cristina Coman[1], Nina Nicole Troppmair[1,2], Mailin-Christin Manke[3,4], Monika Zdanyte[3,4], Tobias Harm[4], Manuel Sigle[4], Dominik Kopczynski[1], Andrea Bileck[1,7], Christopher Gerner[1,7], Nils Hoffmann[8,1], David Heinzmann[4], Alice Assinger[9], Meinrad Gawaz[4], David Stegner[5,6], Harald Schulze[5], Oliver Borst[3,4,11] ✉ & Robert Ahrends[1,11] ✉

During megakaryopoiesis, megakaryocytes (MKs) undergo cellular morphological changes with strong modification of membrane composition and lipid signaling. Here, we adopt a lipid-centric multiomics approach to create a quantitative map of the MK lipidome during maturation and proplatelet formation. Data reveal that MK differentiation is driven by an increased fatty acyl import and de novo lipid synthesis, resulting in an anionic membrane phenotype. Pharmacological perturbation of fatty acid import and phospholipid synthesis blocked membrane remodeling and directly reduced MK polyploidization and proplatelet formation, resulting in thrombocytopenia. The anionic lipid shift during megakaryopoiesis was paralleled by lipid-dependent relocalization of the scaffold protein CKIP-1 and recruitment of the kinase CK2α to the plasma membrane, which seems to be essential for sufficient platelet biogenesis. Overall, this study provides a framework to understand how the MK lipidome is altered during maturation and the effect of MK membrane lipid remodeling on MK kinase signaling involved in thrombopoiesis.

Deriving from pluripotent hematopoietic stem cells in the bone marrow, megakaryocytes (MKs) are responsible for the production of platelets, thus being essential for hemostasis and vascular integrity. Since MKs produce thousands of platelets, irregularities in MK differentiation (megakaryopoiesis) affect platelet generation or function and can result in clinically significant disorders. Thrombocytopenia or impaired platelet function might lead to disrupted primary hemostasis with increased risk of bleeding. In contrast, elevated platelet

[1]Institute of Analytical Chemistry, University of Vienna, Vienna, Austria. [2]Vienna Doctoral School in Chemistry, University of Vienna, Vienna, Austria. [3]DFG Heisenberg Group Cardiovascular Thromboinflammation and Translational Thrombocardiology, University of Tübingen, Tübingen, Germany. [4]Department of Cardiology and Angiology, University of Tübingen, Vienna, Germany. [5]Institute for Experimental Biomedicine, University Hospital Würzburg, Würzburg, Germany. [6]Rudolf Virchow Center for Integrative and Translational Bioimaging, Würzburg, Germany. [7]Joint Metabolome Facility, University of Vienna and Medical University of Vienna, Vienna, Austria. [8]Forschungszentrum Jülich GmbH, Institute of Bio- and Geosciences (IBG-5) Jülich, Jülich, Germany. [9]Institute of Physiology, Centre of Physiology and Pharmacology, Medical University of Vienna, Vienna, Austria. [10]These authors contributed equally: Bianca de Jonckheere, Ferdinand Kollotzek. [11]These authors jointly supervised this work: Oliver Borst, Robert Ahrends. ✉e-mail: oliver.borst@med.uni-tuebingen.de; robert.ahrends@univie.ac.at

counts (thrombocythemia) or excessive platelet activation increases the risk for thrombotic events and ischemic diseases[1].

After the hematopoietic stem cell was discovered more than 150 years ago[2,3], the description of megakaryopoiesis at the omics scale is still in its infancy, although the cellular processes underlying megakaryopoiesis are now well defined[4]. MKs become polyploid during their maturation owing to endomitotic processes and reach diameters of up to 100 µm. However, they only occur with a frequency of 0.2% when compared with other nucleated blood cells, making them difficult to study. The entire process of megakaryopoiesis is accompanied by a substantial membrane reorganization, including shaping a lobulated nuclear envelope, packing granules, generating the lipid-rich demarcation membrane system[5], and MK polarization toward the protrusion of proplatelets into the sinusoids of the bone marrow[6]. Altogether, these processes make it necessary to adapt membrane properties constantly. In particular, sphingolipid metabolism and signaling[7–9] are indicated in the elongation of proplatelet extensions and the shedding process of platelets. Recently, there is growing scientific evidence that de novo lipogenesis may modulate MK maturation and platelet production[10]. It has been reported that maturating MKs incorporate fatty acids (FAs) released by adipocytes closely located to MKs in the bone marrow to facilitate thrombopoiesis[11]. Consequently, the FA transfer from adipocytes to MKs has important clinical implications in obesity-related cardiovascular thrombotic complications.

However, despite its high clinical importance, the MK lipidome composition is still ill defined, and the lipid-dependent processes during MK maturation and platelet biogenesis are largely unknown.

The existence of more than 350 lipids in platelets[12] with the capability to influence membrane geometry and platelet signaling[13] demands a systematic large-scale modulation potential of the lipid metabolism in MKs. Over the last 10 years, mass spectrometry (MS) has evolved into the state-of-the-art technology for lipid analysis. The improvements in sensitivity, speed and resolution, coupled with developments in systems biology[14], ease of access to lipid databases[15] and search engines, and the availability of lipid standards for accurate quantification, have made it possible to explore various aspects of lipid function and regulation[16]. Present-day lipidomics tools provide access to understand lipids' complexity, homeostatic regulation, and role in differentiation, thus linking lipids to diseases and cellular impairments such as platelet dysfunction. Therefore, it is astonishing that neither a quantitative lipid inventory nor a map of the lipid metabolism of MKs is currently available.

Additionally, information gained from multiomics is more valuable when extracted from multiple layers of evidence of one biological sample. This accounts for missing values and points to new molecular mechanisms and interactions. Although lipidomics and proteomics have been successfully applied to investigate different blood cells, the potential of multiomics has yet to be fully explored. Here, we established a multiomics extraction strategy and quantitative MS workflow to determine lipid metabolism and its modulating effect on megakaryopoiesis and proplatelet formation. Using this unique approach, we were able to define regulatory metabolic mechanisms shaping the MK lipidome during MK maturation. These mechanisms directly influence the processes that are critically involved in thrombopoiesis, and their inhibition results in profound thrombocytopenia.

Results

Dynamic lipid metabolism modulation in megakaryopoiesis

For multiomics method development, hematopoietic stem cells were isolated from bone marrow of 10–14-week-old male mice and subjected to a 7-day differentiation protocol. The SIMPLEX workflow (Fig. 1a), which enables simultaneous lipid and protein sample preparation, was used to determine their general molecular composition[17–19]. The differentiation efficiency was monitored by immunocytochemistry staining of the MK surface marker GPIb and the nuclear lobulation using a DRAQ5 DNA stain (Fig. 1b). The MS-based global proteomics analysis was integrated with top-down shotgun and targeted lipidomics to establish the multiomics workflow (Fig. 1a). In total, 4,651 proteins, with two or more unique peptides, were identified and relatively quantified by nano-liquid chromatography (nLC) high-resolution MS. Across the time course of differentiation, comparing all days, 3,152 proteins were significantly regulated, with approximately 1,908 proteins displaying continuous upregulation, 1,189 showing downregulation, and about 55 were transiently regulated. During MK maturation, protein regulation mostly occurred between days 1 and 3, with 593 proteins being upregulated and 455 downregulated (Extended Data Fig. 1a). Computing fuzzy c-means clustering of all regulated proteins ($P < 0.01$) from day 0 to day 7, we identified 39 distinct clusters using a similarity threshold of 85% (Fig. 1c and Extended Data Figs. 2 and 3). Here, 607 proteins showed an overall downward trend, whereas 979 proteins showed an upward trend. In a subsequent pathway enrichment analysis, considering significantly regulated proteins from day 0 to day 7 with a $\log_2$(fold change) of ≥2 or ≤−2 (Fig. 1d), pathway hallmarks of megakaryopoiesis were enriched, such as platelet and extracellular matrix receptor activation (Fig. 1e). However, most strikingly, seven lipid-specific pathways were identified under the top 15 most enriched biosynthesis pathways, ranging from steroid biosynthesis over the PPAR signaling pathway to FA elongation (Fig. 1e), pointing to a strong dependency of MK differentiation on lipid metabolism. The data were particularly analyzed for markers to underscore the enrichment analysis and further evaluate the differentiation process and the discovered link to lipid metabolism. MK differentiation markers such as RUNX1, RUNX3 and GATA1 (refs. 20–22) and surface markers such as GPIb, CD36, VWF, GPV, GPNMB and integrins[23–27] were monitored and shown to be highly regulated (Fig. 1f). Moreover, specific domains of lipid metabolism, such as the FA receptors, transporters, the FA synthetase itself or mitochondrial FA importers are highly upregulated in maturating MKs (Fig. 1g and Extended Data Fig. 1b). Futhermore, the metabolism of complex lipids such as phospholipids, sphingolipids and sterols is elevated, whereas other enzymes derived from oxylipin metabolism were downregulated or unregulated as indicated by their

Fig. 1 | Global proteomics analysis highlights key changes of proteins steering MK maturation. a, Multiomics workflow for the quantitative assessment of the lipidome and proteome of maturating MKs. **b**, Representative immunofluorescence staining of GPIb (platelet glycoprotein Ib β-chain, green) expressed in the late stage of MK maturation and platelets ($n = 6$). Nuclei were stained with DRAQ5 dye (blue). Scale bar, 10 µm (upper panel) or 100 µm (lower panels). **c**, Fuzzy c-means clustering of regulated proteins from day 0 to day 7. Number of proteins and their median are denoted in individual plots, and only a selection of clusters is shown. Note that over 2,229 proteins are not regulated and therefore not considered. The assignment of proteins to clusters can be found in the Source data. Threshold, 85. **d**, Diagram showing nonregulated (light gray) and significantly regulated proteins comparing day 7 versus day 0, with the latter being divided into three sections: upregulated (red) or downregulated (blue) proteins with a $\log_2$(fold change) of ≥2 or ≤−2, respectively, and other regulated proteins (dark gray) with $\log_2$(fold change) between −2 and +2. **e**, Pathway enrichment analysis of significantly regulated proteins with $\log_2$(fold change) of ≥2 or ≤−2 showing the top 15 enriched pathways of only upregulated (red) or downregulated (blue) proteins. Pathways were sorted by their fold enrichment independent of the number of proteins involved. Pathway enrichment analysis was performed using the open-source DAVID bioinformatics tool. **f**,**g**, Bar graphs of various MK differentiation markers (**f**) and lipid-related enzymes (**g**) displayed with their associated lipid category. Proteomics data were combined from three independent experiments with four pooled mice per biological replicate. Means are displayed with the standard deviations represented as error bars. A two-sided *t*-test was used for statistical analysis. Benjamini–Hochberg correction was applied to *P* values using an FDR cutoff of <0.05 (*$P \leq 0.05$; **$P \leq 0.01$; ***$P \leq 0.001$). Oxi, oxylipin.

https://doi.org/10.1038/s44161-023-00325-8

corresponding metabolizing enzymes (Fig. 1g and Extended Data Fig. 1c). Using the latest MS technologies, we assembled a lipid metabolic network of more than 300 proteins involved in lipid transport, synthesis and degradation that shows substantial regulation during MK maturation (Extended Data Fig. 1d). This strong metabolic rewiring at the protein level raised the questions as to what extent this is reflected in the lipidome and if this multiomics-derived information can be used to generate novel hypotheses.

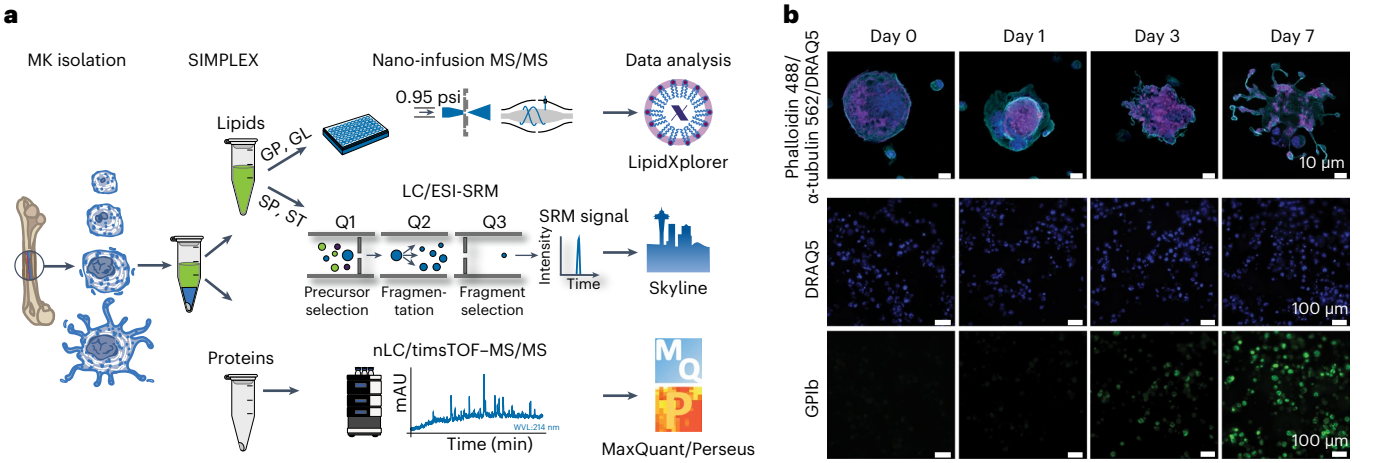

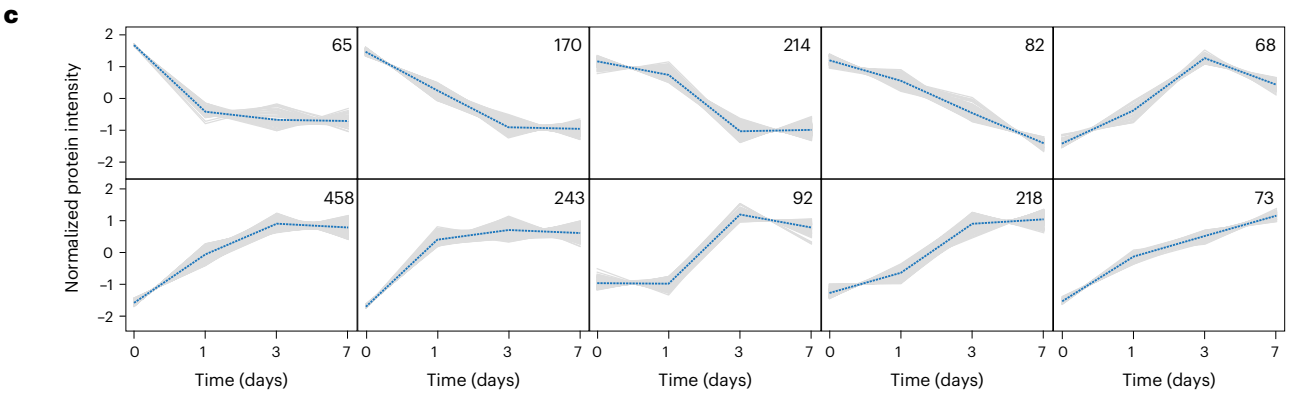

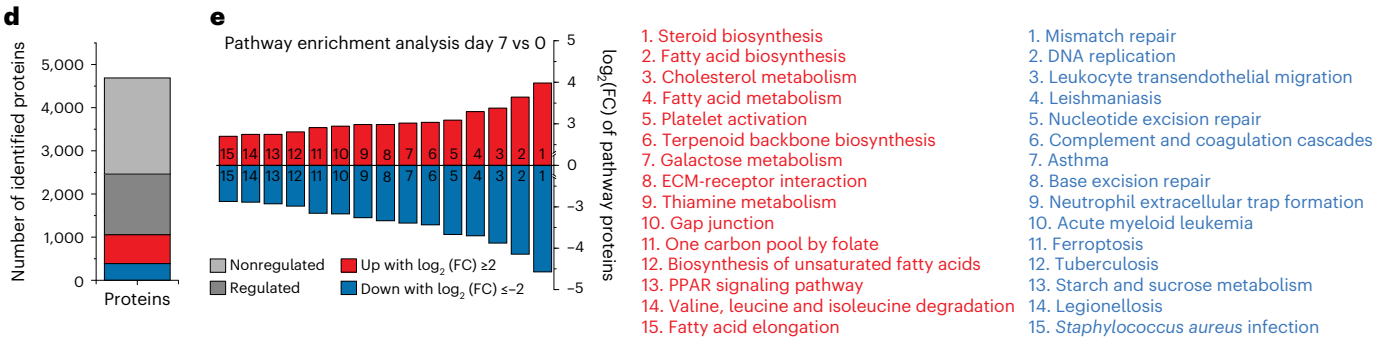

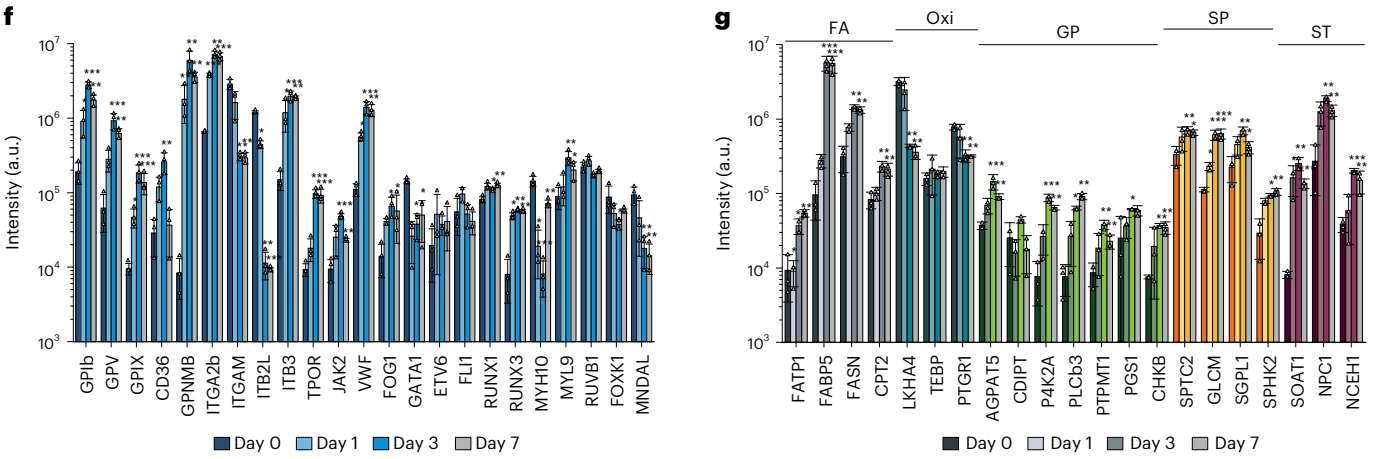

The MK membrane lipidome has specific signatures

For global quantitative lipidomics of MKs during maturation, we used the established workflow (Fig. 1a) integrating shotgun and targeted lipidomics to detect both low-abundant lipid species (for example, ceramides) and major membrane components (for example, glycerophospholipids) simultaneously. All lipid molecules were sequenced and their concentrations were reported using internal standards.

To ensure lipid identification with high confidence, all lipid molecules were structurally characterized by tandem mass spectrometry (MS/MS), enabling the determination of the number of carbon atoms and double bonds for each FA chain (Extended Data Figs. 4 and 5). Knowledge about the FA composition is crucial, as rearrangement and exchange of FAs constantly occur during fundamental cell-fate decisions[28,29] or differentiation[30]. Furthermore, it contributes to the physicochemical features of the membrane, including lateral diffusion and stiffness, but most importantly, it provides the precursor reservoir of many signaling molecules[12,13]. We structurally characterized and identified 473 lipid species in differentiated MKs (Fig. 2) originating from the main lipid categories glycerophospholipid (GP; 343), glycerolipid (GL; 46), sphingolipid (SP; 76) and sterol (ST; 8), thereby covering 24 different lipid classes.

Quantitative lipid analysis was executed using internal standards that co-ionize with the target analyte. Lipids were normalized based on a fixed number of cells and the protein amount. Assembling of the quantitative results revealed a dynamic range of six orders of magnitude similar to the platelet lipidome (Fig. 2a,b)[12]. In mature MKs, low-abundant species such as the signaling molecule sphingoid base phosphate (SPBP) 18:1;O2 (5 pmol mg^{-1}) were detected alongside major structural components such as cholesterol (48,523 pmol mg^{-1}) and PC 16:0_18:1 (11,427 pmol mg^{-1}) (Fig. 2b). Most lipid classes displayed a quantitative distribution of over two orders of magnitude. In contrast, lysophospholipid species, which have signaling capabilities, had a narrower range, likely representing a more tightly controlled metabolism (Fig. 2a). Our evidence shows that 60% of the entire lipid mass is accounted for by 15 lipids, and 70% by 29 lipids (Fig. 2c), making them essential building blocks for the membrane integrity of the MK lipidome.

Compared with platelets, in which 15 lipids already cover 70% of the lipid mass[12], the MK lipidome seems to be twice as complex, with more lipids contributing to membrane properties. The most abundant lipid classes detected within mature MKs were cholesterol (ST), phosphatidylcholine (PC), phosphatidylethanolamine (PE), phosphatidylinositol (PI), phosphatidylserine (PS) and sphingomyelin (SM) (Fig. 2d).

Interestingly, besides arachidonic acid (FA 20:4), which dominated the top 15 lipids in platelets, here eicosatrienoic acid (FA 20:3) is also found under the most abundant molecules in MKs, indicating slight differences in the FA composition of major lipid classes. These differences underscore the likelihood that not only the demarcation membrane system of MKs determines the platelet lipidome, but also subsequent processes such as aging and interaction with the microenvironment during circulation are involved in shaping platelet membranes. Nevertheless, critical precursors for platelet signaling like PI 18:0_20:4 are already abundantly available in MKs. Comparing fully mature MKs against the lipidome of human[31] and mouse[12] platelets reveals an equal basis for various lipid classes such as PE, PS, ST, cholesterol ester (SE), PC-ether lipid (PCO), triacylglycerol (TG) and lyso-PE (LPE) (Fig. 2e). However, PC, PI, and PE-ether lipid (PEO), and especially SP classes such as ceramide (Cer) and hexosylceramide (HexCer), display very distinct abundances. Currently, we can only speculate why this is the case. Platelets lose their ability to synthesize SPs de novo[32]; therefore, higher levels in MKs are likely. Higher Cer levels stabilize Cer-rich platforms, which are needed to preserve multiple signaling processes or to be precursors themselves, steering megakaryopoiesis and thrombopoiesis[9,33].

Anionic membrane remodeling in MK maturation

To gain further insight, we analyzed the MK lipidome on days 1, 3 and 7. Generally, the total membrane content was found to be increased within the first 3 days, as also observed in the lipids-to-protein ratio. Overall, 337 lipids were shared across all days, whereas approximately 10 lipids were distinct for specific days (Fig. 3a). The lipidome seems to be rather stable, as 81% of lipids were not regulated during differentiation (Fig. 3b). The 19% of lipids that were regulated (fold change of ≥2 or ≤−2; $P \leq 0.05$) are mainly derived from low-abundant lipids. Nevertheless, 15 species belonging to 75% of the membrane lipidome are also altered, indicating a change in membrane properties (Fig. 3c). Therefore, we aimed to elucidate higher organizational rearrangements in membranes (Fig. 3d–h). First, we analyzed the coregulation of 506 lipids at the individual molecular lipid species level using absolute concentrations, revealing that most correlated lipids can be found within, but not across, classes (Fig. 3d). Applying the Pearson correlation computed for any lipid pair, 18 distinct clusters of correlated and anticorrelated lipids were identified during differentiation (Fig. 3e). As expected, GPs and SPs were distributed over all clusters, whereas STs were observed only in clusters C8–C13. However, lipid abundance and the individual alterations of each species are difficult to access from a hierarchical view. Therefore, the lipid–lipid correlation matrix was transformed into a network (Fig. 3f–h). Here, most lipid regulation appears between days 1 and 3, and only minor changes can be observed afterward, indicating that the membrane composition is determined relatively early during megakaryopoiesis. Interestingly, similar trends could be observed in the proteomic results (Extended Data Fig. 1a).

To further dissect the reorganization of the MK lipidome during differentiation, we carried out a quantitative analysis at the lipid category, lipid class and molecular species levels, as well as on the corresponding FA composition using absolute concentrations. By investigating the lipidome-wide class-specific representation (Fig. 4a), the results obtained earlier could be emphasized. More specifically, many lipid classes show regulation early on and are rather unchanged in the late stage of differentiation after day 3. Most significantly regulated classes like diacylglycerol (DG), TG, PS, PCO, PE, phosphatidylglycerol (PG), lyso-PG (LPG), PI, lyso-PI (LPI) and sphingoid base (SPB) follow this trend at the class and individual lipid species levels with PG and its lyso forms that are further upregulated at day 7 (Fig. 4b,c). LPI and PCO show opposing trends and are downregulated. Lipids of high interest were validated by high-resolution targeted LC–MS/MS (Extended Data Figs. 6 and 7). To prove that lipid changes are not mirroring the lipid composition of the media or are induced by apoptosis, we analyzed the fetal bovine serum (FBS), determined apoptotic markers, conducted a cell vitality assay, and proved by surface labeling that the PS amount is not increased in the outer membrane leaflet (Extended Data Fig. 8a–d).

Regarding molecular lipid composition, FA shifts can be observed toward a more unsaturated membrane (Fig. 4d,e). However, this is mainly due to an increased level of single monounsaturated FAs rather than total polyunsaturated FAs (PUFAs). Here, a decrease in arachidonic acid with a balancing increase of FA 20:3 can be observed (Fig. 4e). Nevertheless, the total PUFA levels remain unchanged (Fig. 4f). Interestingly, PUFA lipids are more abundant in platelets than in MKs, supporting the hypothesis that the lipidome of platelets is still being formed after release from MKs (Fig. 4f).

Moreover, we observed an increase in odd long-chain FAs (Fig. 4d) from day 1 to day 3, which is likely due to increased branched-chain FAs and their oxidations and unraveled that lysolipids with signaling capabilities such as LPG, lyso-PC (LPC), lyso-PA (LPA) and SPB are upregulated until the end of MK differentiation. Our data reveal that megakaryopoiesis is likely modulated from different mechanisms such as (1) lipidome rearrangement (membrane charge, for example, PG), (2) modulation of the FA lipid composition (membrane fluidity, FA 18:1) and (3) the production of signaling molecules (DG, LPG and SPB).

https://doi.org/10.1038/s44161-023-00325-8

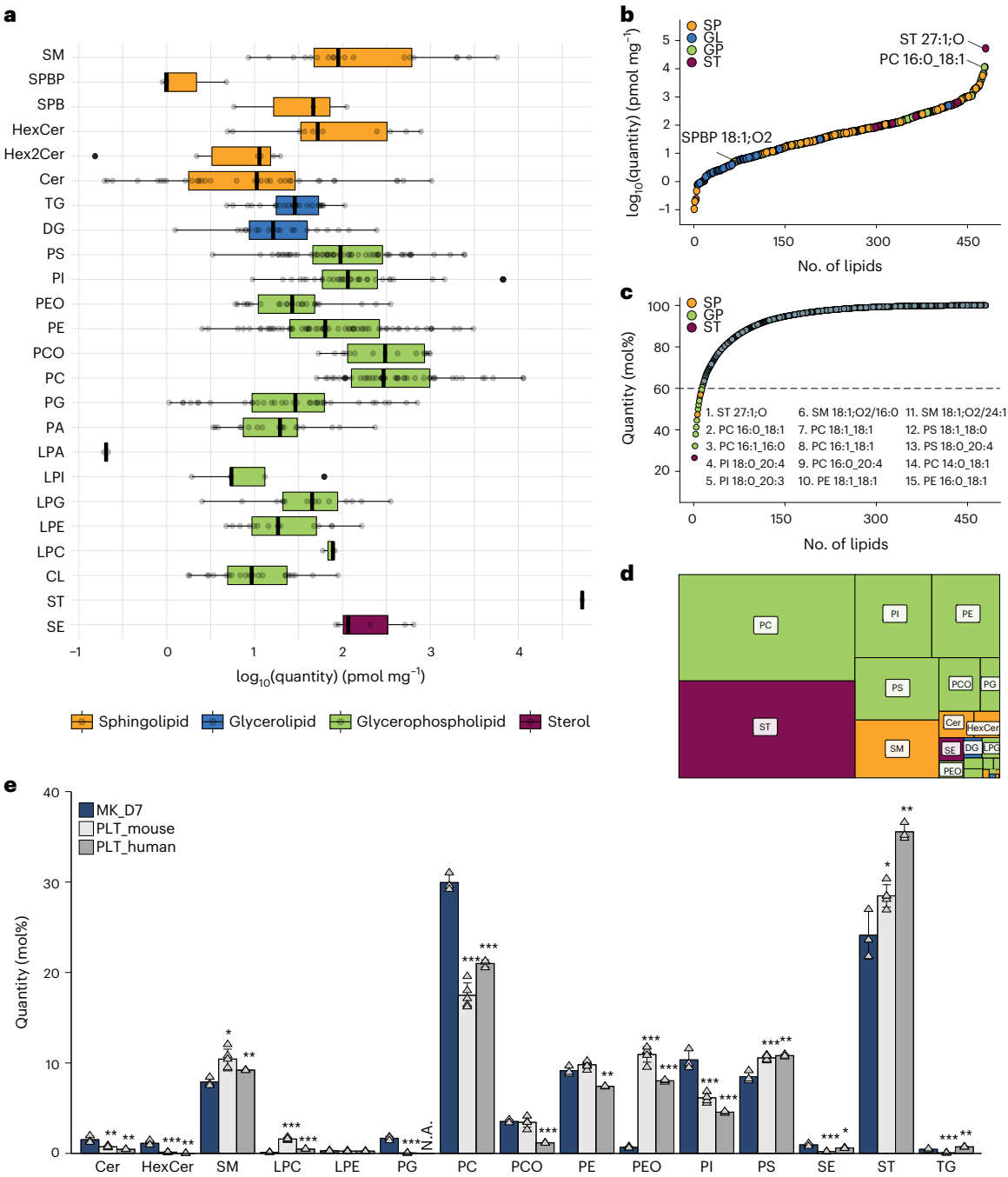

Fig. 2 | Quantitative lipidomics of mature MKs covers a high dynamic range of six orders of magnitude. a, Boxplots displaying the dynamic range of the MK lipidome after 7 days of maturation. Quantities of four lipid categories (SP, GL, GP and ST) spanning 24 lipid classes and 473 lipid species are shown. Each bar is composed of all quantified lipid species within the respective class. **b**, Dynamic range of quantified lipid species covering six orders of magnitude. **c**, Cumulative lipid abundance. Fifteen lipid species account for more than 60% of the total lipid content of mature MKs. **d**, Relative lipid class distribution. Classes are color-coded by category. **e**, Relative distribution of main lipid classes from mature MKs, as well as mouse and human platelets, in mol%. For statistical analysis, a two-sided *t*-test was used, and both platelet samples were tested against MK at day 7 (*$P \leq 0.05$; **$P \leq 0.01$; ***$P \leq 0.001$). All data show the mean of three biological replicates. One biological replicate was comprised of five individual animals. In **a**, boxplot whiskers represent the minimum and maximum, box boundaries represent the 25th and 75th percentiles, and the center line represents the mean. In **e**, error bars represent standard deviations.

Phospholipid synthesis is essential for proplatelet-forming MKs

For validation of our previous data, we inhibited de novo phospholipid biosynthesis at two initiation points (Fig. 5a). In this regard, we added a long-chain acyl-CoA synthetase (ACSL) inhibitor (triacsin C), an inhibitor of glycerol-3-phosphate acyltransferase (GPAT) (FSG67), or vehicle control to the freshly isolated bone marrow cell suspension and collected thrombopoietin (TPO)-stimulated MKs on day 7. Nontreated day-0 MKs were used as baseline control, and changes for all lipid classes were calculated as ratios relative to the control. Treatment with either inhibitor diminished the production of almost all phospholipids, including anionic lipids such as PG, PI and PS (Fig. 5b and Extended Data Fig. 9a). Interestingly, phosphatidic acid (PA) abundances were not altered, indicating a redistribution between lipid classes to preserve PA content. In FSG67-treated MKs, we observed

https://doi.org/10.1038/s44161-023-00325-8

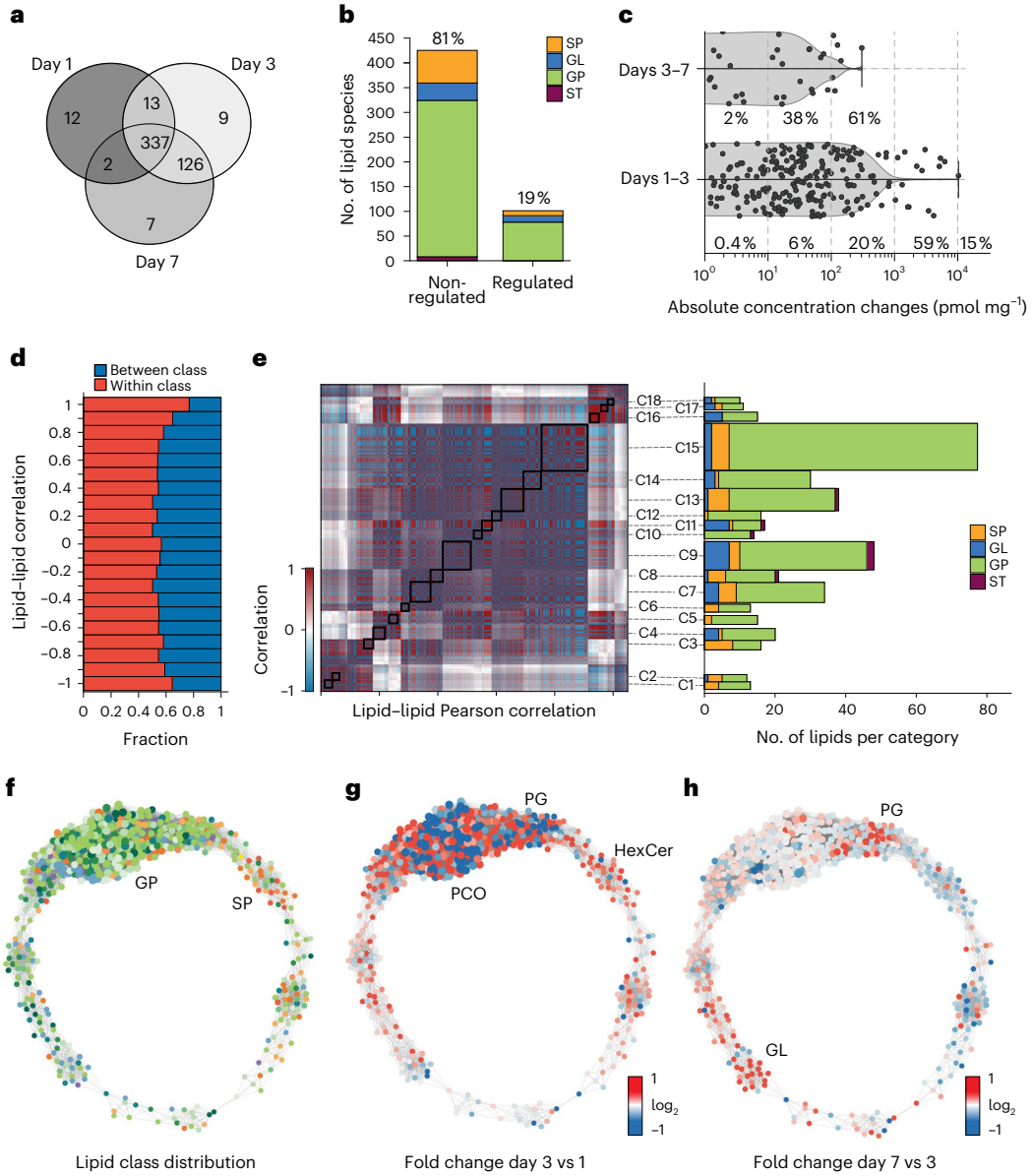

Fig. 3 | Absolute lipid quantification during megakaryopoiesis reveals a stable lipidome and distinct clusters of regulation. a, Venn diagram of shared and distinct lipids across the time course of differentiation. **b**, Bar graph of significant regulated and nonregulated lipids during megakaryopoiesis. **c**, Quantitative proportion of regulated lipids on the overall observed concentration changes. **d**, Analysis of the fraction of correlations connecting lipids of the same lipid class (red) or different lipid classes (blue), as a function of correlation strength. **e**, Hierarchical clustering of the lipid–lipid correlation and anticorrelation matrix. Rows and columns correspond to the 506 quantified lipid species. Black boxes indicate clusters of strongly correlated and anticorrelated lipids with a Pearson correlation coefficient (r) of 0.99 or above. Lipid cluster numbers are indicated on the right. Number of lipids in each cluster are sorted by lipid class. **f**, Network visualization of the lipid–lipid correlations. Nodes are individual lipid species. Edges are correlations or anticorrelations ($r \geq 0.99$). Node size represents the degree of connectivity, and node color represents the analyzed lipid class. **g**,**h**, The network during differentiation. Fold change was mapped onto the generated network and day 1 compared to day 3 (**g**) and day 3 to day 7 (**h**). The displayed pure red indicates a fold change of ≥2, and pure blue indicates a fold change of ≤−2. Data are combined from three independent biological experiments, and mean values are shown.

slightly, but not significantly, decreased levels of DG and an increase in PC. Of note, TGs increased 3-fold compared with day-7 control, likely owing to the production of lipid droplets to compensate for high levels of acyl-CoA within the cell. Whereas phospholipid biosynthesis is hampered when inhibitors are used, the production of SM and ST appears to be enhanced. This could be owing either to an excess of serine and palmitoyl-CoA that cannot be incorporated via normal lipogenesis, or to SM and ST acting as functional substituents of other stabilizing membrane lipids. To elucidate the role of phospholipids in MK maturation, we first monitored control and inhibitor-treated MKs and visually examined their ability to form proplatelets. MKs were taken after 3 days of differentiation, and proplatelet formation was observed for 30 h. The number of proplatelet-forming MKs increased by only 9% for FSG67-treated and triacsin C-treated MKs, instead of 20% as observed for control MKs (Fig. 5c,d). Further, polyploidization of inhibitor-treated MKs was markedly impaired as reflected by a significant reduction of polyploidy and a significantly higher percentage of MKs with DNA content of <8 N (Fig. 5e). Both inhibitors resulted in an overall greatly reduced number of proplatelet-forming cells compared with the control, indicating that proper MK development and proplatelet formation

https://doi.org/10.1038/s44161-023-00325-8

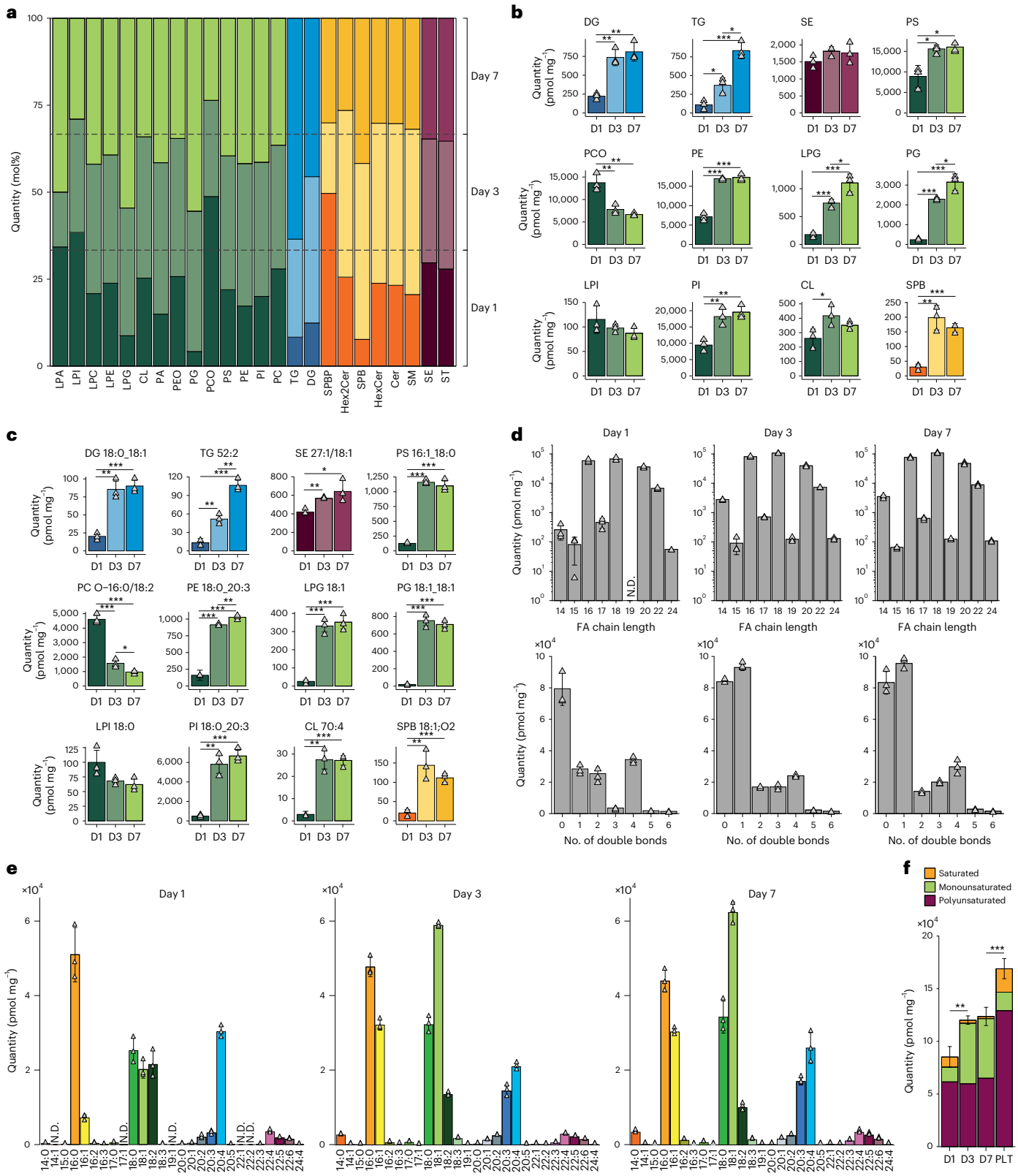

Fig. 4 | Quantitative lipid inventory analysis of MKs reveals shifts in FA and double bond distribution during the course of MK maturation. a, Relative lipid class distribution at different time points (dark, day 1; light, day 3; medium, day 7) of MK maturation. **b**, Absolute concentrations of selected lipid classes. D1, day 1; D3, day 3; D7, day 7. **c**, Selected lipid species, each representing the corresponding class displayed in **b**. **d**, Amount and distribution of FA chain length (number of carbon atoms) (top) and double bonds (bottom) of GPs on days 1, 3 and 7 of MK maturation. **e**, Bar graphs of FA absolute abundances derived from different GP species. **f**, Absolute quantification of the saturated, monounsaturated and polyunsaturated FA content of GPs during megakaryopoiesis (on days 1, 3 and 7) and in platelets (PLT). All data show the mean of three biological replicates. One biological replicate was comprised of five individual animals. Error bars represent standard deviations. In **f**, error bars represent summed standard deviations of the total FA content each day. A two-sided *t*-test was used for statistical analysis (*$P \leq 0.05$; **$P \leq 0.01$; ***$P \leq 0.001$).

requires both de novo lipid synthesis and uptake of exogenous FAs from dietary lipids.

These results could also be translated into in vivo conditions. Treatment of mice with either inhibitor over a period of 7 days resulted in a significant reduction in the MK sinusoid contact, with a significantly higher rate of MK fragmentation within the bone marrow of murine femora and reduced polyploidy (Fig. 5f,g and Extended Data Fig. 9b). These marked effects on thrombopoiesis resulted in significant thrombocytopenia in inhibitor-treated mice compared with mice treated with solvent control (Fig. 5h,i). Notably, in vivo visualization of MKs in the bone marrow of the mouse skull using two-photon intravital microscopy (2P-IVM) unraveled a profound reduction of the ratio of proplatelet-forming MKs in bone marrow of mice treated with FSG67 (6.6 ± 3.7%) or triacsin C (10.6 ± 3.1%) compared with vehicle-treated mice (14.4 ± 5.5%), indicating that both treatments impair proplatelet formation in vivo (Fig. 5h and Extended Data Fig. 9c) and consequently result in thrombocytopenia (Fig. 5i) Moreover, 2P-IVM revealed an increased ratio of MKs with altered morphology and premature ectopic fragmentation (triacsin C, 6.5 ± 2.1%; FSG67, 8.6 ± 3.0%; vehicle, 4.5 ± 2.4%), potentially resulting in an inefficient proplatelet release into the vascular sinusoids.

Anionic membrane regulates platelet biogenesis via CKIP-1/CK2α axis

Finally, we investigated how class rearrangement to a more anionic membrane, through increase of PG, PI and PS, can increase the anionic lipid strength in MKs from 13 mol% to 20 mol% (0.2–1.7 mol%, 7.5–10.8 mol% and 7–8.8 mol%, respectively). Thereby, increased signaling capability could potentially modulate megakaryopoiesis. Therefore, we reanalyzed our proteomics data with an interaction analysis and identified a network of 67 strongly regulated kinases, as well as additional 162 regulated proteins containing at least one of the following lipid-binding domains: pleckstrin homology (PH) or PH-like domains[34]; C1 and C2 (refs. 35,36); four-point-one, ezrin, radixin, moesin (FERM) domains[37]; or Src homology domains SH2 or SH3, which were recently identified to also show lipid-binding capabilities[38]. All have a strong link to anionic lipids[37,39–42]. Among those proteins, we identified several kinases that themselves harbor lipid-binding sites such as Janus kinases 1 and 2 (JAK1/JAK2), integrin-linked protein kinase (ILK), Bruton's tyrosine kinase (BTK), protein kinase C-α (PKC-α) and several Src family kinases such as SRC, FYN and LYN (Extended Data Fig. 10a–c). All eight are linked to megakaryocytic development and platelet activation[43–45] and interact with or are directly or indirectly activated by lipids[46–49].

Given that anionic phospholipids linked to membrane binding exhibit continuous upregulation, we speculate whether the interplay of lipids, lipid-binding proteins and kinases may act as a potential modulatory axis driving megakaryopoiesis and proplatelet formation. Using the Molecular Complex Detection (MCODE)[50] clustering algorithm within the open-source software Cytoscape[51], we were able to identify six clusters (cutoff score, 2.0) of densely connected regions in the protein interaction network (Fig. 6a). Whereas clusters 1, 2, 4 and 5 were closely clustered together, clusters 3 and 6 showed clear separation. Interestingly, cluster 6 was formed by the casein kinase 2 catalytic subunits (CK2α/CK2α′), the CK2 regulatory β-subunit (CK2β), and the adapter protein PH domain-containing family O member 1/casein kinase interacting protein-1 (PKHO1/CKIP-1).

In this context, we identified a robust upregulation of the CKIP-1/CK2 cluster during megakaryopoiesis on day 7 (Fig. 6b). CKIP-1 reflects an adapter protein with a PH domain facilitating recruitment of the CK2α isoform to the plasma membrane via direct interaction resulting in nonenzymatic regulation of CK2α activity[52–54]. CKIP-1 contains a PH domain at the amino terminus and five proline-rich motifs throughout the protein, which mediate multiple cellular protein interactions[55]. Immunoblotting revealed a strong upregulation of the membrane localization of CKIP-1 in MKs and its coexpressed target CK2α at day 7 (Fig. 6c), an effect that was abolished in MKs treated with ACSL inhibitor triacsin C or the GPAT inhibitor FSG67, respectively. These observations suggest a regulation of the CKIP-1/CK2α interplay at the MK plasma membrane by the ACSL/GPAT lipid metabolic axis during megakaryopoiesis. To elucidate the functional role of the recruited catalytic CK2α subunit for the process of thrombopoiesis, we examined MK localization and morphology in immunostained bone marrow cryosections of intact murine femora from mice with an MK-specific or platelet-specific genetic deletion of CK2α (*csnk2α1*). The visualization of MK distribution within the entire femora confirmed that MKs in the femora of *csnk2α1*$^{Pf4\Delta/Pf4\Delta}$ mice displayed less direct sinusoidal contact and conversely an accumulation of MKs in the bone marrow hematopoietic compartment with markedly increased MK fragmentation (Fig. 6d and Extended Data Fig. 10d), pointing to insufficient transendothelial platelet biogenesis. Additionally, investigation of MKs flushed out of bone marrow revealed a significantly reduced ploidy in *csnk2α1*$^{Pf4\Delta/Pf4\Delta}$ MKs, with a significant reduction of ≥16 N-containing MKs (Fig. 6e), indicating that *csnk2α1* deficiency results in the accumulation of immature MKs. To study the effect of genetic deletion of CK2α in MK-dependent thrombopoiesis, we performed in vitro proplatelet formation assays using MKs derived from the bone marrow of *csnk2α1*$^{Pf4\Delta/Pf4\Delta}$ mice and *csnk2α1*$^{lox/lox}$ littermates. Accordingly, significantly fewer numbers of *csnk2α1*$^{Pf4\Delta/Pf4\Delta}$ MKs formed proplatelets (Fig. 6f). Thus, abolished MK maturation and proplatelet formation again contribute to the development of significant macrothrombocytopenia in *csnk2α1*$^{Pf4\Delta/Pf4\Delta}$ mice when compared with *csnk2α1*$^{lox/lox}$ mice (Fig. 6g). Altogether, these observations let us hypothesize that the lipid-driven CKIP-1/CK2α axis in MKs is crucial for MK maturation and proplatelet formation (Fig. 6h).

Discussion

Megakaryopoiesis is a complex process by which hematopoietic stem cells differentiate into MKs, which are eventually capable of releasing

Fig. 5 | Inhibition of de novo phospholipid biosynthesis pathways leads to reduced MK polyploidization and proplatelet formation. a, Schematic representation of FA uptake and phospholipid biosynthesis pathways. Acyl-CoA is generated from FAs via long-chain ACSL and transferred into glycerol-3-phosphate (G3P) by GPAT to create LPA. Inhibitors of the enzymatic steps are shown as red inhibitory arrows. Dashed arrows connect lipids to anionic lipid shift illustrating putative functions in proplatelet formation. **b**, Relative amount of depicted lipid classes of control and inhibitor-treated MKs (triacsin C or FSG67) on day 7. Nontreated day-0 MKs were used as baseline control, and lipid quantities were set to 1. Standard deviations are depicted as dashed lines. Changes for all lipid classes were calculated as ratios relative to control at day 0. **c**, Number of proplatelet-forming cells in vitro of control and inhibitor-treated MKs examined from day 4 for 30 h (means ± s.d.; $n = 5$). **d**, Representative images of proplatelet-forming MKs after 24-h examination. **e**, Representative ploidy histogram and arithmetic means of DNA content of control and inhibitor-treated CD41$^+$ bone marrow-derived MKs cultured for 5 days ($n = 6$). **f**, Representative confocal microscopy images of immunostained femora cryosections (left) and arithmetic means ± s.d. ($n = 6$; right) of MK localization (distance to sinusoids) and fragmentation in the bone marrow of mice subjected to DMSO, triacsin C or FSG67 injections for 7 days. Green, MKs (GPIb); red, sinusoids (CD105); blue, nuclei (DRAQ5). Asterisks indicate fragmented MKs. **g**, Representative ploidy histogram and arithmetic means of DNA content of bone marrow MKs from triacsin C-treated, FSG67-treated or vehicle-treated mice ($n = 5–7$). **h**, Representative median projections of 25-µm z-stacks (left) and arithmetic means ± s.d. ($n = 5–7$; right) of MK fragmentation and proplatelet-forming MKs from the bone marrow of triacsin C-treated, FSG67-treated or vehicle-treated mice. Arrows indicate proplatelets, and asterisks indicate fragmented MKs. Green, MKs/platelets (GPIX derivative); magenta, vessels (CD105). Graphs represent ratios of proplatelet-forming (left) and fragmented MKs (four to eight z-stacks per mouse). **i**, Platelet count of triacsin C-treated, FSG67-treated or vehicle-treated mice ($n = 9$). A two-sided *t*-test was used for statistical analysis (*$P \le 0.05$; **$P \le 0.01$; ***$P \le 0.001$).

https://doi.org/10.1038/s44161-023-00325-8

platelets into the bloodstream through a process called thrombopoiesis. It is characterized by a progressive increase of cellular dimensions, DNA content with subsequent polyploidization, and, finally, proplatelet formation into the bone marrow sinusoids.

Recently, a few studies tried to shed light on how lipid metabolism can affect megakaryopoiesis and proplatelet formation by mainly investigating enzymes derived from SP metabolism[7,9,32]. Nevertheless, these studies did not elucidate the chemical nature of the involved

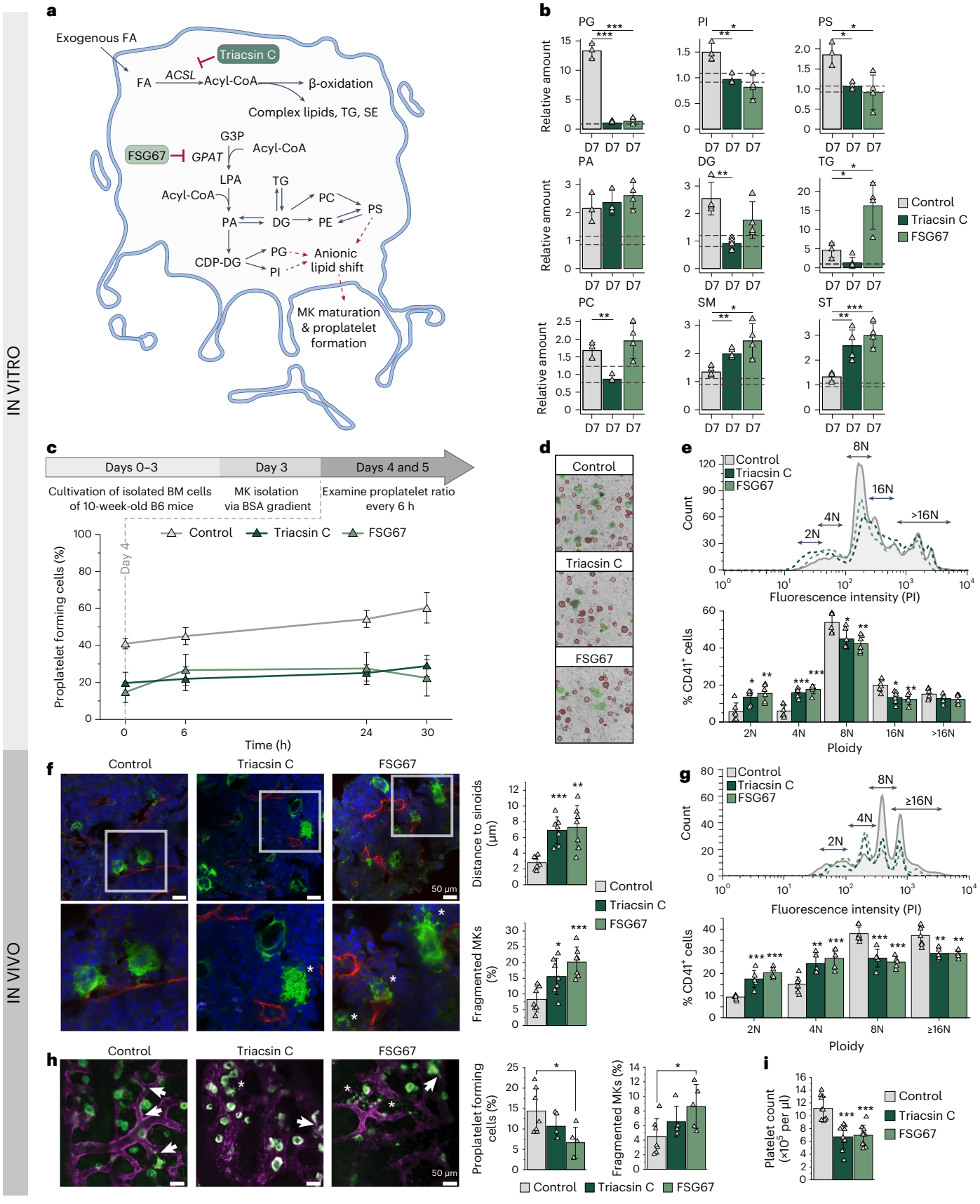

https://doi.org/10.1038/s44161-023-00325-8

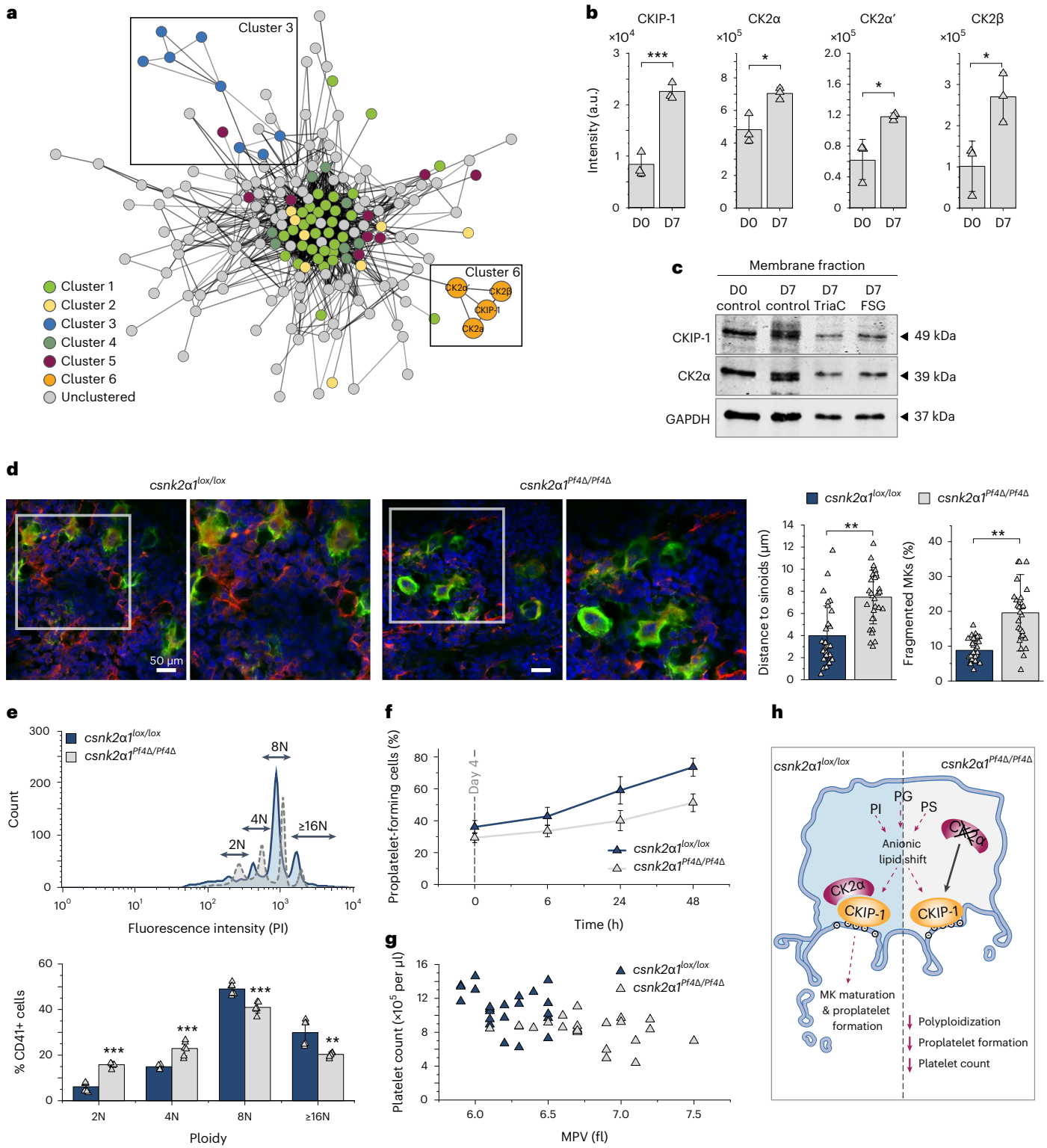

Fig. 6 | During MK maturation, PKHO1/CKIP-1 and CK2α are increasingly recruited to the MK plasma membrane, and genetic deletion of *csnk2α1* in MKs results in reduced ploidy and disrupted proplatelet formation with macrothrombocytopenia. a, Network cluster analysis using MCODE. Edges are correlations with a minimum interaction confidence score of 0.5. Nodes are proteins. Node colors represent the associated cluster. **b**, Regulation of proteins of cluster 6, showing relative protein intensities. Arithmetic means ± s.d. ($n = 3$) are shown. **c**, Immunoblot analysis of CKIP-1 and CK2α protein levels in the membrane fraction of day-7 MKs treated with either triacsin C or FSG67 ($n = 5$). **d**, Representative confocal microscopy images of immunostained femora (left) and arithmetic means ± s.d. ($n = 6$; right) of MK fragmentation and distance to sinusoids in the bone marrow of *csnk2α1*$^{lox/lox}$ and *csnk2α1*$^{Pf4Δ/Pf4Δ}$ mice. Green, MKs (GPIb); red, sinusoids (CD105); blue, nuclei (DRAQ5). **e**, Representative ploidy histogram and arithmetic means ± s.d. ($n = 6$) of DNA content of *csnk2α1*$^{lox/lox}$ and *csnk2α1*$^{Pf4Δ/Pf4Δ}$ bone marrow-derived MKs cultured for 5 days. **f**, Number of proplatelet-forming cells of *csnk2α1*$^{lox/lox}$ and *csnk2α1*$^{Pf4Δ/Pf4Δ}$ MKs examined from day 4 for 48 h (means ± s.d.; $n = 6$). **g**, Count and mean platelet volume (MPV) of *csnk2α1*$^{lox/lox}$ and *csnk2α1*$^{Pf4Δ/Pf4Δ}$ platelets ($n = 22$). Each triangle represents one individual mouse. **h**, Hypothetical illustration of obtained results showing reduced ploidy, proplatelet formation and platelet count in *csnk2α1*-deficient mice. A two-tailed *t*-test was used for statistical analysis (*$P \leq 0.05$; **$P \leq 0.01$; ***$P \leq 0.001$).

https://doi.org/10.1038/s44161-023-00325-8

lipid species to describe the observed functional effects leading to pathologies such as thrombocytopenia. Therefore, it is still unclear if lipids are the actual cause of the functional effect. To investigate the exact mechanisms of lipidome regulation during megakaryopoiesis, lipids must be analyzed in detail simultaneously with their metabolizing proteins. Several aspects should be considered, for example, time and sensitivity of cell isolation, using detergent-free conditions, and reporting of concentrations to understand the dimensions of membrane rearrangement under the given circumstances. Here, we have used the full technological advancement of MS-based lipidomics to report a quantitative lipidomics map of MK differentiation using a lipid-centered multiomics approach[18]. On the one hand, we quantified 473 lipid species covering a concentration range of over six orders of magnitude. On the other hand, the expression levels of around 4,651 proteins were determined. Using one sample to cover multiple molecule classes reduces the analytical error and enhances the correlation between different molecules[17]. Quantitatively, the MK lipidome seems twice as complex as the one derived from platelets[12,56]. Additionally, PUFAs are less enriched in the MK membrane compared with platelets. Nevertheless, both lipidomes are comparable, which is reflected in the abundance of different lipid classes. The higher complexity of the MK lipidome is most likely based on the presence of more organelles and an advanced lipid metabolism.

Using a multiomics approach to dissect megakaryopoiesis, this study revealed three major findings. First, lipid uptake is highly increased during MK maturation, which is reflected by the increased expression of FA receptors (CD36 and FATP1) and transporters (FABP4/5). Second, FA synthesis and oxidation are elevated in differentiating MKs, indicated by the upregulation of FA synthetase (FASN) and different mitochondrial FA transporters needed for β-oxidation, such as CPT2 and CACP (Extended Data Fig. 1b). Third, a significant remodeling of complex lipid synthesis pathways such as SP, GP and ST occurs, which can be observed at the enzyme and lipid levels. Interestingly, increasing TG levels indicate an elevated lipid droplet formation, most likely needed for β-oxidation. Most lipidome changes occur between days 1 and 3, demonstrating that membrane remodeling is an early process during megakaryopoiesis. However, the most striking finding was the upregulation of anionic membrane lipids, which increased by >7 mol% during differentiation. Of note, this elevation in anionic lipid mass correlated well with the upregulation of DG. As a result of pharmacological inhibition of FA uptake or GP de novo synthesis, no upregulation of anionic lipids in maturating MKs was observed. Moreover, the inhibition of either ACSL or GPAT resulted in impaired MK polyploidization and perturbated thrombopoiesis reflected by a 50% reduction of proplatelet formation and release into the bone marrow sinusoids resulting in a significant thrombocytopenia.

Using relative quantitative proteomics, we uncovered a broad spectrum of proteins whose expression was significantly shifted during the early and late stages of megakaryopoiesis. A recent study compared the proteome and transcriptome of round versus proplatelet-producing MKs by two-dimensional (2D) electrophoresis and polysome profiling to uncover protein changes during megakaryopoiesis[57]. Using the latest MS technology, we analyzed the proteome at several time points of megakaryopoiesis and proplatelet formation. This enabled us to assess abundances of over 4,400 proteins, compared with 200 proteins in the previously mentioned study. Of the 30 proteins previously identified to be regulated, most also displayed regulation in our study. Due to the increased sensitivity of our approach, more than 3,000 proteins were found to be regulated. Remarkably, we unraveled several proteins and kinases that could potentially be regulated by (anionic) lipids and are significantly regulated during megakaryopoiesis. A signaling pathway that was significantly upregulated in MKs during MK maturation was the CKIP-1/CK2 cluster. The regulatory β-subunit of CK2 has been reported as major regulator of MK maturation and thrombopoiesis[58].

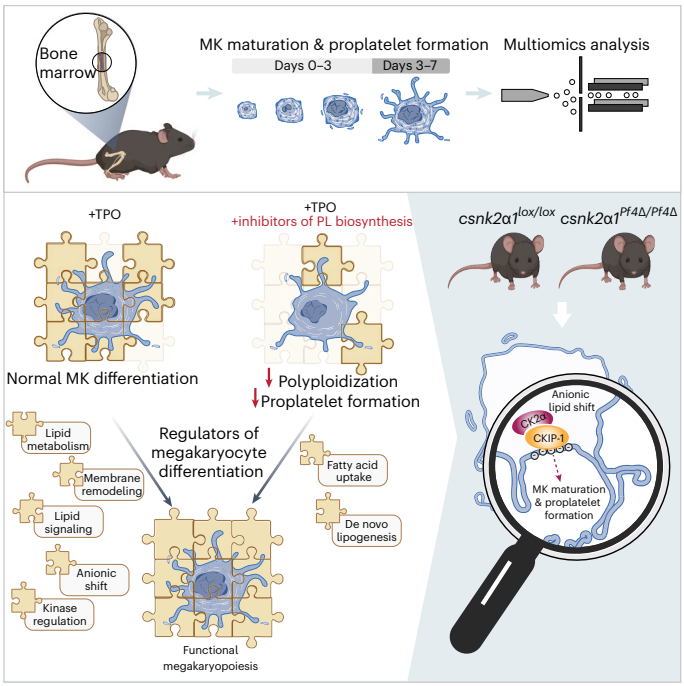

Fig. 7 | Lipid-driven functional regulation and underlying mechanisms of MK maturation and thrombopoiesis. This study focuses on the functional analysis and regulation of MK maturation and proplatelet formation, using a multiomics approach and incorporating both in vitro and in vivo methodologies. To develop the multiomics method, we isolated hematopoietic stem cells from murine bone marrow and subjected them to a 7-day differentiation protocol with TPO. The SIMPLEX workflow, which enables simultaneous lipid and protein sample preparation, was used to comprehensively determine the general molecular composition of MKs. The results revealed significant anionic lipid membrane remodeling and relocalization of the CKIP-1/CK2α complex to the plasma membrane, which appear to be essential for adequate platelet biogenesis. The graphical illustration was generated using BioRender.

CKIP-1 is a nonenzymatic and specific regulator of the catalytic CK2α isoform activity[52]. CKIP-1 binds to the plasma membrane via its PH domain by specific binding of anionic lipids such as PS, PI and PI's phosphorylated forms[53,54]. Furthermore, CKIP-1 controls the access of CK2α to specific cellular targets through its ability to selectively recruit CK2α and not CK2α′ to the plasma membrane, again in a PH domain-dependent manner[52]. Accordingly, we unraveled CKIP-1/CK2α as a potential effector of the lipidome remodeling downstream of ACSL and GPAT. The anionic shift of the MK lipidome during MK maturation culminates in an increase of phospholipids that are able to bind to the PH domain of CKIP-1 with consecutive recruitment of CKIP-1 and CK2α to the plasma membrane of MKs. It has been reported that CKIP-1 is crucially involved in MK differentiation and thrombopoiesis, and a genetic deletion of CKIP-1 (*plekho1/ckip1*) resulted in defective megakaryopoiesis with reduced MK ploidy and reduced platelet production with significant thrombocytopenia[59]. Similarly, after MK-specific or platelet-specific genetic deletion of CK2α (*csnk2a1*), we found significantly reduced MK ploidy and abrogated proplatelet formation with the development of significant macrothrombocytopenia. Remarkably, *csnk2a1*$^{Pf4\Delta/Pf4\Delta}$ mice displayed a highly comparable pattern of MK distribution within the bone marrow, the same MK characteristics with premature fragmentation, and reduced proplatelet formation with subsequent thrombocytopenia as mice upon treatment with the ACSL or GPAT inhibitor (Fig. 7).

These identified mechanisms in MK maturation and thrombopoiesis are of potential interest to deepen our understanding of how alterations in lipid metabolism in diseases such as obesity or metabolic

syndrome, both associated with thrombotic cardiovascular complications, might interfere with platelet production.

In this study, we aimed to establish an MK-specific multiomics workflow to comprehensively analyze MK lipid metabolism. We demonstrated that the MK lipidome remodeling during MK maturation and proplatelet formation involves ACSL-dependent or GPAT-dependent lipid metabolism. As a result from a shift toward anionic membrane properties during MK maturation, the altered MK lipidome may promote specific signaling complexes and kinases, such as CKIP-1/CK2α, that are critically involved in thrombopoiesis. However, further analyses linking anionic membrane remodeling to kinase changes in proplatelet formation are ultimately warranted to tackle the question of how lipids control platelet production and properties.

Methods

Materials and standards

Antibodies. Rabbit anti-α-tubulin (Thermo Fisher Scientific, PA5-19489), rat anti-CD42b monoclonal (clone Xia.G7, Emfret, M042-1), rat FITC anti-mouse CD41 (BioLegend, 133904), rabbit anti-CSNK2A1 (Abcam, ab76040), mouse anti-CKIP-1 (Santa Cruz Biotechnology, sc-376355), mouse anti-GAPDH (Thermo Fisher Scientific, MA5-15738), goat anti-rabbit secondary antibody (Life Technologies, A21069), goat anti-rat secondary antibody (Life Technologies, A11006), donkey anti-mouse secondary antibody (LI-COR, 926-32212), Alexa Fluor 594-conjugated anti-CD105 antibody (BioLegend, 120418), Alexa Fluor 546-conjugated anti-CD105 (self-generated, clone MJ7/18, ref. 60), anti-CD42a (GPIX) Alexa Fluor 488 derivative (self-generated, p0p6, ref. 61).

Chemicals. DRAQ5 DNA stain (Thermo Fisher Scientific, 62251), Alexa Fluor 488 phalloidin (Life Technologies, A12379), antibody diluent (Zytomed, ZUC025-100), Roti-Load (Roth, K929.1), bovine serum albumin (BSA) (PanReac AppliChem, A1391,0500), triacsin C (Cayman Chemical, 10007448), FSG67 (Focus Biomolecules, 10-4577), mounting medium (Invitrogen, P36961), poly-L-lysine (Sigma-Aldrich, P8920-100ML, 0.1%), paraformaldehyde (PFA) (Otto Fischar GmbH & Co. KG, 27246), Cell Lysis Buffer (Cell Signaling Technology, 9803S), Protease/Phosphatase Inhibitor Cocktail (Cell Signaling Technology, 5872S), FcR Blocking Reagent mouse (Miltenyi Biotec, 130-092-575), PureLink RNase A (Invitrogen, 12091-021), propidium iodide (Invitrogen, P1304MP), EZ-Link Sulfo-NHS-Biotin (SNB) (Thermo Fisher Scientific, 11851185), EZ-Link NHS-Biotin (NB) (Thermo Fisher Scientific, 10381394), L-lysine (Sigma-Aldrich, L5501), triethylamine (Sigma-Aldrich, 90335), medetomidine (Pfizer), midazolam (Roche), fentanyl (Janssen-Cilag), recombinant TPO (ImmunoTools, 12343615).

Chemicals specific for lipid analysis: formic acid (BioSolve, 6914143), ULC/MS-grade methanol (BioSolve, 13684102), ULC/MS-grade water (BioSolve, 23214102), ULC/MS-grade acetonitrile (ACN) (BioSolve, 1204102), methyl *tert*-butyl ether (MTBE) (VWR, 34875-1L), ammonium acetate (Merck, 73594-25G-F), ammonium formate (Sigma-Aldrich, 70221-25G-F), HPLC-grade phosphoric acid (Sigma-Aldrich, 79617-250ML, 85–90%), chloroform (Sigma-Aldrich, 650498-1L), isopropanol (IPA) (Sigma-Aldrich, 1010402500).

Chemicals specific for protein analysis: formic acid (VWR, 84865-180P), ULC/MS-grade methanol (VWR, 83638320), ULC/MS-grade water (Honeywell, 14263-2L), ULC/MS-grade ACN (Honeywell, 34967-2.5L), urea (Merck, 1084871000), triethylammonium bicarbonate (TEAB) (Sigma-Aldrich, 18597-100ML), sodium dodecyl sulfate (SDS) (GERBU, 1212), dithiotreitol (DTT) (Sigma-Aldrich, APOSBIMB1015-25G), iodoacetamide (IAA) (Sigma-Aldrich, I6125-25G), Trypsin/Lys-C Mix Mass Spec Grade (Promega, V5073), trifluoroacetic acid (TFA) (Sigma-Aldrich, T6508-100ML).

Peptide standards. Standard peptide [Glu^1]-Fribrinopeptide B (sequence EGVNDNEEGFFSAR, Sigma-Aldrich, F3261), standard peptide M48 (sequence TTPAVLDSDGSYFLYSK, PSL), standard peptide HK0 (sequence VLETKSLYVR, PSL), standard peptide HK1 (sequence VLETK(ε-AC)SLYVR, PSL).

Lipid standards. Mouse SPLASH LIPIDOMIX Mass Spec Standard (Avanti Polar Lipids, 330710X-1EA) consisting of PC 15:0-18:1(d7), PE 15:0-18:1(d7), PS 15:0-18:1(d7), PG 15:0-18:1(d7) (as internal standard for PG and CL), PI 15:0-18:1(d7), PA 15:0-18:1(d7), LPC 18:1(d7), LPE 18:1(d7) (as internal standard for all lysophospholipids except LPC), SE 18:1(d7), PC-ether (PCO-a) 18:0-18:1(d9), PE-ether (PEO-a) 18:0-18:1(d9), DG 15:0-18:1(d7), TG 15:0-18:1(d7)-15:0 and SM d18:1-18:1(d9); Ceramide/Sphingoid Internal Standard Mixture II (Avanti Polar Lipids LM6005-1EA) consisting of sphingosine (SPB) d17:1, sphinganine (SPB) d17:0, sphingosine-1-P (SPBP) d17:1, sphinganine-1-P (SPBP) d17:0, SM d18:1/12:0, Cer d18:1/12:0, glucosylceramide (GlcCer) d18:1/c12:0 (as internal standard for HexCer), lactosylceramide (LacCer) d18:1/12:0 (as internal standard for dihexosylceramide (Hex2Cer)) and ceramide-1-P (CerP) d18:1/12:0; cholesterol-d7 (Avanti Polar Lipids, 700041P); lysosphingomyelin (LSM)-d7 (Avanti Polar Lipids, 860639P); PS 14:0-14:0 (Avanti Polar Lipids, 840033P) (self-generated biotinylated internal standard for biotin-PS).

Animal models

Csnk2a1$^{lox/lox}$ mice were generated elsewhere[62]. For MK-specific or platelet-specific deletion of CK2α, *csnk2a1*$^{lox/lox}$ mice were crossed with Pf4-Cre transgenic mice (The Jackson Laboratory, 008535) and studied at the age of 12–14 weeks. All animal experiments were performed according to Directive 2010/63/EU of the European Parliament on the protection of animals used for scientific purposes and were approved by local authorities (Regierungspräsidium Tübingen) following the ARRIVE guidelines (protocols M01/20G and M03/19M).

For in vivo treatment studies, 6-week-old C57BL6/J mice, were treated daily intraperitoneally with either 0.285 mg per kg (body weight) triacsin C, 5 mg per kg (body weight) FSG67 or dimethylsulfoxide (DMSO) over a period of 7 days. Concentrations were adapted according to refs. 63,64.

Bone marrow isolation and MK differentiation

For the bone marrow isolation, a centrifugation protocol previously published by ref. 65 was used. Briefly, 10–14-week-old, male C57BL/6J mice (The Jackson Laboratory) were anesthetized using isoflurane and killed by cervical dislocation following the institutional guidelines and the German law for the welfare of animals. Both femora were dissected and cleaned, cut open at the knee side, and placed with the cut side facing down in a 0.5-ml Eppendorf tube with a pre-pierced hole in the bottom. The tube was placed into a 1.5-ml tube, pre-filled with 100 µl of DMEM (supplemented with 1% penicillin/streptomycin and 10% FBS) and centrifuged for 1 min at 2,600 × *g* at room temperature (21°C (69.8°F)). Next, 1 ml of supplemented medium was added, and bone marrow cells were resuspended, then filtered through a pluriStrainer Mini (70 µm), and the strainer was rinsed with 1 ml of medium. Afterward, cells were centrifuged for 5 min at 300 × *g* at room temperature, and the supernatant was removed.

To induce MK differentiation, the freshly isolated bone marrow cells (pool of five individual animals) were cultivated in 10-cm cell culture dishes containing supplemented DMEM, and differentiation was initiated by adding (1%) recombinant TPO. Cells were cultivated at 37 °C, 5% CO_2 for different periods of time. On days 1, 3 and 7, cells were collected (1,000 r.p.m., 5 min) and resuspended in 950 µl of PBS. The cell suspension was carefully pipetted on a two-phase BSA gradient (bottom, 1.5 ml 3% BSA in PBS; top, 1.5 ml 1.5% BSA in PBS) to separate cells by weight. After 40 min, the supernatant was removed, and the cell pellet was washed three times with 500 µl of PBS. Cells were counted in a Neubauer chamber and adjusted to 200,000 cells per tube. Cell pellets were shock-frozen in liquid nitrogen and stored at −80 °C for later multiomics analysis.

Immunofluorescence microscopy

For immunofluorescence microscopy of MKs, cells were isolated and purified as described above and cultivated for 1, 3 and 7 days. After isolation via BSA gradient, 5,000 MKs were seeded on chamber slides precoated with 0.1% poly-L-lysine for 60 min at 37 °C and further incubated for 1 h. Cells were fixed for 15 min with 4% PFA at room temperature, washed three times for 3 min each with PBS, 10 min with PBS and 0.1% Triton X-100, and again three times for 3 min each with PBS. Cells were further incubated with 1% BSA in PBS to block the unspecific binding of antibodies. Cells were stained with either the primary antibodies Alexa Fluor 488 phalloidin (1:200 in antibody diluent) and α-tubulin (1:400 in antibody diluent) or CD42b (1:100 in antibody diluent), or CD42d (1:300 in antibody diluent). After overnight incubation at 4 °C and washing three times for 3 min each with PBS, secondary antibodies (anti-rabbit Alexa Fluor 568, 1:300 in PBS; anti-rat Alexa Fluor 488, 1:300 in PBS) were applied for 2 h at room temperature. After three washes for 3 min each with PBS, nuclei were stained for 15 min with DRAQ5 stain (1:1,000), washed again with PBS, and mounted using a mounting medium. An LSM510 confocal laser scanning microscope (Zeiss) and ZEN Blue software (Zeiss) were used for the analysis.

Protein and lipid extraction

Samples, consisting of 200,000 cells per tube, were used for lipid and protein extraction following the SIMPLEX protocol previously described by ref. 18. In brief, 225 µl of methanol and the internal standard mixture were added to all samples, and cell pellets were homogenized through 2–5 min of ultrasonication. Two blanks used as quality controls were processed in parallel, one with and the other without internal standards. Next, 750 µl of MTBE were added, and samples were incubated for 1 h at 950 r.p.m. at 4 °C. To induce phase separation, 188 µl of water (HPLC-grade) were added, and samples were incubated on ice for 5 min. After a 10-min centrifugation step at 10,000 × *g* at 4 °C, the upper organic phase (containing GPs, GLs, SPs and STs) was carefully removed and dried under a gentle nitrogen flow. The dried organic phase was reconstituted in 100 µl of IPA/methanol/$CHCl_3$ (4:2:1, v/v/v) containing 7.5 mM ammonium acetate for lipid analysis. To complete protein precipitation, 527 µl of methanol were added to the lower aqueous phase, and samples were stored for 2 h at −20 °C, following centrifugation for 30 min at 12,000 × *g* at 4 °C. The protein pellet was dried and further subjected to protein analysis.

Protein analysis

Proteomics sample preparation. Protein samples were diluted 1:2 in lysis buffer (8 M urea, 50 mM TEAB, 5% SDS), then heated at 90 °C for 5 min, and protein concentrations were determined using a Pierce BCA Protein Assay Kit (Thermo Scientific). For enzymatic digestion, 20 µg of protein were used, and ProtiFi S-Trap technology was applied[66]. In short, solubilized proteins were reduced and carbamidomethylated by adding 64 mM DTT and 48 mM IAA, respectively. Before loading the samples onto S-Trap mini cartridges (ProtiFi), trapping buffer (90% (v/v) methanol, 0.1 M TEAB) was added. Subsequently, samples were thoroughly washed and then digested using Trypsin/Lys-C Mix for 2 h at 37 °C. Finally, peptides were eluted, dried, and stored at −20 °C until LC–MS analysis.

Label-free proteomics. LC–MS/MS analysis was performed as described previously[67–69]. In brief, reconstitution of dried peptide samples was achieved by adding 5 µl of 30% formic acid containing four synthetic standard peptides. Afterward, samples were diluted with 40 µl of loading solvent (97.9% H_2O, 2% ACN, 0.05% TFA), of which 5 µl were injected into the Dionex UltiMate 3000 nano high-performance liquid chromatography (HPLC) system (Thermo Fisher Scientific). A pre-column (2 cm × 75 µm, PepMap 100 C18, Thermo Fisher Scientific) run at a flow rate of 10 µl min^{-1} using mobile phase A (99.9% H_2O, 0.1% formic acid) was used to pre-concentrate peptides before chromatographic separation. Peptides were then separated on an analytical column (25 cm × 75 µm, 25 cm, Aurora Series emitter column, IonOpticks) by applying a flow rate of 300 nl min^{-1} and using a gradient of 8–40% mobile phase B (79.9% ACN, 20% H_2O, 0.1% formic acid) over 155 min, resulting in a total LC run time of 195 min including washing and equilibration steps. A timsTOF Pro mass spectrometer (Bruker) with a captive spray ion source run at 1,700 V was used for MS analysis. The timsTOF Pro was operated in parallel accumulation–serial fragmentation (PASEF) mode, and moderate MS data reduction was applied. Further parameters included a scan range (m/z) from 100 to 1,700 to record MS and MS/MS spectra and a 1/k0 scan range of 0.60–1.60 V.s/cm^2 resulting in a ramp time of 100 ms to achieve trapped ion mobility separation. All experiments were performed with ten PASEF MS/MS scans per cycle, leading to a total cycle time of 1.16 s. Furthermore, the collision energy was ramped as a function of increasing ion mobility from 20 eV to 59 eV, and the quadrupole isolation width was set to 2 Th for $m/z < 700$ and 3 Th for $m/z > 700$. All samples were analyzed in technical duplicates.

Label-free proteomics data analysis. The publicly available software package MaxQuant (v1.6.17.0) running the Andromeda search engine was used for protein identification and label-free quantification (LFQ)[70]. Therefore, raw data were searched against the Swiss-Prot database *Mus musculus* (v220621 with 17,519 entries). Search parameters included an allowed peptide tolerance of 20 ppm, a maximum of two missed cleavages, carbamidomethylation on cysteines as fixed modification, methionine oxidation, and N-terminal protein acetylation as variable modification. A minimum of two peptides per protein, of which at least one has to be unique for each protein, was set as a search criterium for positive identifications. In addition, the 'match between runs' option was applied, using a 0.7-min match time window, a match ion mobility window of 0.05, a 20-min alignment time window, and an alignment ion mobility of 1. A false discovery rate (FDR) of ≤0.01 was set for all peptide and protein identification. LC–MS data evaluation and statistical analysis were accomplished using the Perseus software (v1.6.14.0)[71]. Identified proteins were first filtered for reversed sequences and common contaminants and annotated according to differentiation time points. Before statistical analysis, LFQ intensity values were log_2-transformed, means of technical duplicates were calculated, and proteins were additionally filtered for their number of independent identifications (a minimum of three identifications in at least one group). Two-sided *t*-tests and statistics for volcano plots were performed by applying an FDR cutoff of 0.05 and an S0 of 0.1, whereby S0 controls the relative importance of the *t*-test *P* value and difference between the means. Figure visualization was done using OriginPro (v2021), RStudio (v1.4.1106) and Instant Clue (v0.10.10)[72].

Protein network and cluster analysis. For the generation of protein networks, we divided our proteomics data into two groups: kinases and lipid-binding proteins. All proteins that were significantly regulated on either day were used for network analysis using STRING. Networks generated were loaded in Cytoscape (v3.9.1). For protein clustering, the MCODE application inside the Cytoscape interface was used with the following conditions: network scoring including loops with a degree cutoff of 2, cluster finding with fluffing using a node density cutoff of 0.8 and node score cutoff of 0.24 with K-core of 2 and max depth of 100.

Lipid analysis

Shotgun lipidomics. A Q Exactive HF (Thermo Fisher Scientific) coupled to a TriVersa NanoMate ion source (Advion Biosciences) was used for direct infusion experiments. A total of 12 µl of the sample were delivered over 14 min with a backpressure of 0.95 psi. After 6 min, polarity switching from +1.25 kV to −1.25 kV was applied to acquire mass spectra in both positive and negative ion modes in one measurement. Full MS spectra covering the mass range of 350–1200 m/z in both positive and

negative modes were acquired with a resolution of 240,000, an AGC target of 1e6, and a maximum IT of 105 ms. MS1 acquisition was followed by data-independent acquisition of precursor masses at an interval of 1,001 Da. The precursor isolation window was 1 Da, and normalized collision energy (nCE) was 21% and 26% for positive and negative modes, respectively. MS2 spectra were acquired with a resolution of 60,000, an AGC target of 1e5, and a maximum IT of 105 ms.

Targeted lipidomics. Analysis of SP and ST was performed as previously described by ref. 73. Inclusion lists for targeted measurements were generated using LipidCreator (v1.2.0). For the reversed-phase LC, the UltiMate 3000 system was equipped with an Ascentis Express C18 main column (150 mm × 2.1 mm, 2.7 µm, Supelco) and fitted with a guard cartridge (50 mm × 2.1 mm, 2.7 µm, Supelco) in a column oven set to 60 °C. Solvent A was ACN/H_2O (3:2, v/v), solvent B was IPA/ACN (9:1, v/v), and both contained 0.1% formic acid, 10 mM ammonium formate and 5 µM phosphoric acid. The separation was carried out with a flow rate of 0.5 ml min^{-1} with the following 25-min-long gradient: initial, 30% B; 0–2 min, hold 30% B; 2–3 min, 30–56.1% B; 3–4 min, 56.1–58.3% B; 4–5.5 min, 58.3–60.2% B; 5.5–7 min, 60.2–60.6% B; 7–8.5 min, 60.6–62.3% B; 8.5–10 min, 62.3–64% B; 10–11.5 min, 64–64.5% B; 11.5–13 min, 64.5–66.2% B; 13–14.5 min, 66.2–66.9% B; 14.5–15 min, 66.9–100% B; 15.0–19.0 min, hold 100% B; 19 min, 5% B; 19–22 min, hold 5% B; 22 min, 30% B; 22–25 min, hold 30% B. The injector needle was automatically washed with 30% B and 0.1% phosphoric acid, and a volume of 5 µl per sample was injected.

The LC was coupled to a QTRAP 6500+ (Applied Biosystems Sciex) with an electrospray ion source (Turbo V ion source). MS scans were acquired in positive ion mode with the following source settings: curtain gas, 30 arbitrary units; temperature, 250 °C; ion source gas I, 40 arbitrary units; ion source gas II, 65 arbitrary units; collision gas, medium; ion spray voltage, +5,500 V; declustering potential, +100 V/−100 V; entrance potential, +10 V; exit potential, +13 V. For the scheduled multiple reaction monitoring, Q1 and Q3 were set to unit resolution. The detection window was set to 2 min, and the cycle time was set to 0.5 s. Data were acquired with Analyst (v1.7.2, Applied Biosystems Sciex).

Lipid identification and quantification. All spectra from shotgun experiments were converted to centroid mode using msConvert (v3.0.20186-dd907d757) and analyzed using LipidXplorer (v1.2.8.1) under the following settings: MS1, mass tolerance of 5 ppm with an intensity threshold of 1e5; MS2, mass tolerance of 10 ppm with an intensity threshold of 5e4. For lipid identification, molecular fragmentation query language queries, based on the previous work from refs. 74,75, were compiled to match precursor and fragment ions to recognize lipid species. The detection and quantification of GLs (DG and TG) were used in positive ion mode. GPs (cardiolipin (CL), LPA, LPI, LPG, LPC, LPE, PA, PG, PC, PCO, PE, PEO, PI and PS) were identified and quantified in negative ion mode. All signal intensities were normalized to the corresponding deuterated internal standard (Mouse SPLASH LIPIDOMIX Mass Spec Standard). Protein concentrations, determined by the Pierce BCA Protein Assay Kit, were used to quantify all lipid species. TGs and CLs were quantified based on precursor intensities (Supplementary Table 1).

SPs (Cer, HexCer, Hex2Cer, Sulfo-HexCer (SHexCer), LSM, SPBP, SPB and SM) and STs (ST and SE) were identified and quantified by LC–MS analysis (Supplementary Table 2). Integration of peaks from targeted measurements was performed using Skyline (v21.1.0.146). Lipid species abundance was calculated using peak areas and quantified to the respective internal standard (Ceramide/Sphingoid Internal Standard Mixture II; cholesterol-d7) and protein amount described above.

Generation of biotinylated PS standards

A biotinylated PS internal standard was generated for quantification of biotin-labeled PS species within the biological sample. The generation of biotinylated standards was performed according to the protocol of ref. 76. In brief, 1 mg of PS 14:0_14:0 standard (Avanti Polar Lipids) was dissolved in 330 µl of chloroform/methanol (2:1, v/v), and 6 mg of NB were added. After vortexing, 3.3 µl of triethylamine (Sigma) were added and incubated for 30 min at room temperature. Excess NB was sedimented by centrifugation for 5 min at 500 × *g* at room temperature. The supernatant was transferred into a new glass vial. The sediment was washed once with 330 µl of 2:1 $CHCl_3$/methanol, vortexed and centrifuged, and the supernatant was combined from the previous step. After drying under nitrogen flow, the biotinylated standard was resuspended in 600 µl of methanol for HPLC purification. An Agilent 1200 Series LC system with a Discovery C18 column (250 mm × 4.6 mm, 5 µm) was used with the following conditions: temperature, 22 °C; flow rate, 1 ml min^{-1}; gradient elution profile, 50% B (A, water + 5 mM ammonium acetate; B, methanol + 5 mM ammonium acetate) to 100% B over 15 min, held at 100% B for 20 min, then re-equilibrated to 50% B. Ultraviolet absorbance was measured at 205 nm. Six times, 100 µl were injected and all fractions were manually collected, combined and dried using a Genevac and resuspended in 200 µl of methanol. The standard was transferred into a clean, pre-weighted glass vial, dried and weighted again. The standard concentration was adjusted to 100 ng $µl^{-1}$ in methanol and stored under nitrogen gas at −80 °C. The derivatization of the standard was validated by direct injection on an amaZon speed ion ETD trap instrument.

Surface labeling of externalized PS

Biotinylation of cell surface-exposed PS was performed based on the protocol from ref. 76. A cell-impermeable reagent (SNB) was used to label PS on the outer leaflet, and a cell-permeable reagent (NB) was used for quantification of total PS content. In brief, MK cell suspensions containing 200,000 cells per sample were equally divided in two tubes (100,000 cells each) and treated with either 43 µl of 22 mM SNB in PBS or 20 µl of 20 mM NB in DMSO for 10 min at room temperature. To SNB-treated cells, 72 µl of 250 mM L-lysine in PBS were added and incubated for another 10 min at room temperature to quench excess SNB. To NB samples, 95 µl of LC-grade water were added to reach the final extraction volume of 315 µl. Samples were transferred into 5-ml polypropylene Eppendorf tubes and subjected to the SIMPLEX protocol as described in the section 'Protein and lipid extraction' using a tripled amount of all solvents. For normalization of lipid intensities, 10 µl of a self-generated biotinylated PS standard (biotin-PS 14:0_14:0, 10 ng $µl^{-1}$) and 5 µl of Mouse SPLASH mix (Avanti Polar Lipids) were added prior to extraction. Dried lipid extracts were resuspended in 25 µl of butanol solvent (1-butanol:IPA:H_2O, 8:23:69, v/v/v + 5 mM phosphoric acid), and lipids were identified using targeted LC–MS/MS.

Reversed-phase LC–MS/MS of biotinylated PS

Lipid extracts were separated by reversed-phase HPLC according to ref. 77 with minor adaptions. For separation, an Ascentis Express C18 column (150 mm × 2.1 mm, 2.7 µm, Supelco) fitted with a guard cartridge (50 mm × 2.1 mm, 2.7 µm, Supelco) was used. Mobile phase A was ACN/H_2O (60:40, v/v), mobile phase B was IPA/ACN (90/10, v/v), and both contained 10 mM ammonium formate and 0.1% formic acid. The temperatures of the autosampler and the column oven were set to 10 °C and 60 °C, respectively. Separation was carried out with a flow rate of 0.5 ml min^{-1} with the following 35-min-long gradient: initial, 30% B; 0.0–3.0 min, hold 30% B; 3.0–15.0 min, ramp to 75% B; 15.0–17.0 min, ramp to 100% B; 17.0–30.0 min, to 5% B; 30.1–35.0 min, to 30% B. The injector needle was automatically washed with 30% B, and a volume of 5 µl per sample were injected.

The LC was coupled to the Q Exactive HF instrument, and data were acquired in negative ion mode. The following electrospray ionization (ESI) source parameters were applied: spray voltage, 3.8 kV; capillary temperature, 270 °C; sheath gas flow rate, 50; auxiliary gas flow rate, 15; auxiliary gas heater temperature, 380 °C; S-lens RF level, 60. Full MS spectra from 500 to 1,200 *m/z* were acquired in negative mode with a

resolution of 60,000, an AGC target of 106, and a maximum IT of 50 ms. For MS/MS, a resolution of 30,000, an AGC target of 105, a maximum IT of 115 ms and an nCE of 24 were applied.

Identification and quantification of biotinylated PS

Integration of peaks from targeted measurements was performed using Skyline (v21.1.0.146). The top two abundant PS species (PS 18:0_18:1 and PS 18:0_20:4) were monitored. For the identification of biotinylated PS, both FAs and the neutral loss of the biotinylated PS headgroup (*m/z*, 313) were used. Lipids were quantified on the MS1 level. Lipid species abundance was calculated using peak areas and quantified to the respective internal standard (biotinylated PS to B-PS 14:0_14:0, unlabeled PS to PS 15:0_18:1(d7)). To account for differences in PS total amount throughout the samples, the summed intensity of labeled and unlabeled PS within each sample were used to normalize the amount of labeled PS. A ratio was calculated of externalized:total PS. Day 1 was set to 1 and used as a reference to calculate relative changes during megakaryopoiesis.

Validation of shotgun lipidomics data by targeted LC–MS/MS

Trends of selected lipid species shown in Fig. 4c were validated by targeted LC–MS/MS to increase confidence in the data obtained by shotgun lipidomics. After extraction of lipids by SIMPLEX, the dried lipid phase was resuspended in 50 µl of butanol solvent (1-butanol:IPA:H_2O, 8:23:69, v/v/v + 5 mM phosphoric acid) and separated by reversed-phase LC–MS/MS. LC parameters are as described in the section 'Reversed-phase LC–MS/MS of biotinylated PS.' The LC was coupled to the Q Exactive HF instrument applying the following ESI source parameters: spray voltage, 4.0 kV and 3.8 kV in positive and negative modes, respectively; capillary temperature, 270 °C; sheath gas flow rate, 50; auxiliary gas flow rate, 15; auxiliary gas heater temperature, 380 °C; S-lens RF level, 60. GLs were analyzed in positive mode, and GPs were analyzed in negative mode. Except for TG and CL, all lipids were quantified on the MS2 level. High-resolution MS full scan and parallel reaction monitoring were performed in one measuring cycle (MS1: 0.0–35.0 min negative mode, resolution 60,000, 350–1500 *m/z*; 13.0–35.0 min positive mode, resolution 30,000, 400–900 *m/z*; MS2: 0.0–16.0 min negative mode, resolution 30,000, nCE 24; 13.0–16.0 min positive mode, resolution 30,000, nCE 21). An AGC target of 10^6 and 10^5 and a maximum IT of 50 ms and 115 ms were used in full scan and parallel reaction monitoring, respectively. A pooled sample was measured in both polarities separately to verify the identification and acquire MS2 data for TG and CL.

Visualization and network analysis

For further investigation of common patterns in the lipid profiles, we performed both similarity-based clustering and network analysis based on the analysis approach of ref. 12. In the first step, we compared all lipids with each other pairwise. For each lipid, we computed the mean abundances for days 1, 3 and 7, which we denote as a lipid profile. For each lipid pair, we compared their lipid profiles using Pearson correlation. The result is a quadratic similarity matrix *m*. For the network analysis, we have drawn a graph in which we connected all lipids with each other that had a cosine similarity ≥99% in *m*. For the cluster analysis, we sorted *m* row-wise and column-wise equally. To do so, we applied hierarchical clustering on the columns of *m* with cosine similarity and unweighted average clustering. The result is a sorted matrix *m*. Since we were interested in lipid profiles even with anticorrelation, we worked only with the absolute values of *m*. Along the diagonal of the sorted matrix *m*, we searched for the biggest nonintersecting squared areas, where all values within the squares have a Pearson correlation value of ≥99%. The results are presented in Fig. 3e–h. Networks were generated using Cytoscape (v3.9.1).

Cell vitality assay

Cell vitality of control and inhibitor-treated MKs was determined by a Promega CellTiter-Glo 2.0 Assay, based on the quantification of ATP and indication of metabolically active cells, as done in ref. 78. Experiments were performed according to the manufacturer's protocol. Per 96 wells, 10,000 MKs were seeded in TPO-supplemented DMEM. Inhibitors of phospholipid synthesis (160 µM FSG67, 5 µM triacsin C), 1 µM ionomycin or DMSO were added to the cells in single wells and cultivated for 0, 3 and 7 days. Ionomycin was added to cells as a positive control for apoptotic cells. Plates were equilibrated to room temperature for approximately 30 min before the addition of CellTiter-Glo 2.0 reagent (equilibrated to 22 °C). The reagent was added to each well in a 1:1 ratio of reagent:cell culture medium, mixed and incubated for 2 min on an orbital shaker to induce cell lysis. After 10 min, luminescence signals were recorded using a GloMax-Multi Detection System (Promega, 9300-002).

Subcellular protein fractionation

Subcellular protein fractions were obtained using the Subcellular Protein Fractionation Kit for Cultured Cells (Thermo Scientific, 78840) following the manufacturer's instructions with some modifications. MKs were isolated after cultivation for 0 days and 7 days in TPO-supplemented DMEM and washed with ice-cold PBS. One hundred thousand cells were pelleted by centrifugation for 2 min at 500 × *g*. Cell pellets were dried, 100 µl of ice-cold CEB containing protease inhibitors (1:100) were added, and cell pellets were incubated for 30 min at 4 °C while mixing on an end-over-end shaker. After centrifugation for 5 min at 500 × *g*, the supernatant was collected, and to the remaining cell pellet, 100 µl of ice-cold MEB containing protease inhibitors (1:100) were added, vortexed for 5 s and incubated for 10 min at 4 °C while mixing. The supernatant (membrane fraction) was collected after 5 min of centrifugation at 3,000 × *g* and frozen at −80 °C until immunoblot analysis.

Immunoblot analysis

Immunoblot analysis was performed using the prepared membrane fraction of cultivated MKs (day 0 and day 7) in the absence or presence of the inhibitors. After centrifugation for 15 min at 20,000 × *g* at 4 °C, the supernatant was collected, and the protein concentration was measured using a Bradford assay from Bio-Rad. For immunoblotting, protein was loaded in 12% gels and electrotransferred onto a nitrocellulose membrane, followed by blocking with 5% nonfat milk or 5% BSA for 1 h at room temperature. Afterward, the membrane was incubated with the primary antibody against CSNK2A1 (1:1,000), PKHO1/CKIP-1 (1:200) or GAPDH (1:1,000) overnight at 4 °C. After washing with TBS-T, the blots were incubated with fluorochrome-conjugated secondary antibodies (1:15,000) for 1 h at room temperature. After washing, antibody binding was detected with an Odyssey infrared imaging system (LI-COR). Bands were quantified with ImageJ (National Institutes of Health)[79].

Functional assessment of megakaryopoiesis

To validate the importance of the observed lipidomic changes on megakaryopoiesis, inhibitors of two enzymes involved in phospholipid biosynthesis were used. We added 160 µM FSG67, 5 µM triacsin C or vehicle control (DMSO) to the cell suspensions 24 h after the start of cultivation.

Lipidomic analysis (see the section 'Lipid analysis') was performed on MKs isolated via BSA gradient on day 0 (before the addition of inhibitors and control) and after 7 days of cultivation.

Proplatelet formation assay

Proplatelet formation assays were performed in triplicates on 48-well plates. After isolation via BSA gradient after 3 days of cultivation, 15,000 cells per well were seeded. Proplatelet formation was examined every 6 h by microscopy (ECLIPSE Ti2, NIS-Elements imaging software, Nikon). Ratios of proplatelet-forming MKs compared with non-proplatelet-forming MKs were calculated.

MK polyploidization

Ploidy measurements were performed according to ref. 1. In brief, the bone marrow of femora from B6 mice was flushed and homogenized. Cells were cultivated in 10-cm cell culture dishes containing DMEM (supplemented with 1% penicillin/streptomycin and 10% FBS), and differentiation was initiated by adding (1%) recombinant TPO. After 5 days of cultivation, the cell suspension was carefully pipetted on a two-phase BSA gradient (bottom, 1.5 ml 3% BSA in PBS; top, 1.5 ml 1.5% BSA in PBS) to separate cells by weight. After 40 min, the supernatant was removed, and the cell pellet was washed three times with 500 µl of PBS. Nonspecific bone marrow binding was blocked by incubation with 0.02 mg ml^{-1} FcR Blocking Reagent. Afterward, MKs were stained using FITC-conjugated anti-CD41 antibody, and the cells were subsequently washed once with 2 mM EDTA in PBS. Then, cells were washed with PBS (5 min at 300 × *g*) and fixed in PBS containing 1% PFA/0.1% EDTA. Fixed cells were washed with PBS (10 min at 300 × *g*) and permeabilized in PBS containing 0.1% Triton X-100. Finally, DNA was stained using 50 µg ml^{-1} propidium iodide staining solution containing 100 µg ml^{-1} RNase A and 2 mM EDTA in PBS. Analysis was performed by flow cytometry (BD FACSCalibur, BD Biosciences) and FlowJo software (Tree Star, Inc.) (Supplementary Fig. 1).

2P-IVM

Mice were anesthetized by intraperitoneal injection of 0.5 mg per g (body weight) medetomidine, 5 mg per g (body weight) midazolam and 0.05 mg per g (body weight) fentanyl. A 1-cm midline incision was made to expose the frontoparietal skull, while carefully avoiding damage to the bone tissue. For immobilization of the head, the mice were placed on a custom-built metal stage equipped with a stereotactic holder. Bone marrow vasculature was visualized by injection of anti-CD105 Alexa Fluor 546 (0.6 µg per g (body weight)), and MKs and platelets were visualized by injection of anti-CD42a (GPIX) Alexa Fluor 488 derivative (0.8 µg per g (body weight)). Images were acquired on an upright two-photon fluorescence microscope (TCS SP8 MP, Leica Microsystems) equipped with a ×25 water objective with a numerical aperture of 1.0. A tunable broadband Ti:sapphire laser (Chameleon, Coherent) was used at 780 nm to capture Alexa Fluor 488 and 546 fluorescence. For each mouse, four to eight z-stacks with a step size of 0.51 µm were recorded from different positions in the bone marrow. Proplatelet-forming MKs were counted, and MK morphology was categorized as normal or fragmented by a blinded experimenter. ImageJ was used to generate movies (Supplementary Videos 1–3).

Immunofluorescence staining on femora cryosections

Femora of inhibitor-treated or *csnk2α1*$^{lox/lox}$ and *csnk2α1*$^{Pf4\Delta/Pf4\Delta}$ mice were fixed with 4% PFA in 5 mM sucrose solution (Sigma-Aldrich), transferred into 10% sucrose in PBS and dehydrated using a graded sucrose series (10%–20%–30%). Subsequently, femora were embedded in Cryo-Gel (Leica) and shock-frozen in liquid nitrogen. Cryosections with a thickness of 5 µm were generated using a CryoJane Tape Transfer System (Leica) and probed with a self-conjugated FITC-anti-CD41 antibody (1:100) for specific labeling of MKs and platelets, Alexa Fluor 647-conjugated anti-CD105 antibody (1:300) for endothelium detection, and DRAQ5 (1:1,000) for nuclei staining. Samples were visualized using a Leica Stellaris 5 (LMB R039a) confocal microscope.

Reporting summary

Further information on research design is available in the Nature Portfolio Reporting Summary linked to this article.

Data availability

Data have been deposited at MetaboLights (MTBLS6082, MTBLS6083 and MTBLS6084) and the Proteomics Identification Database (PRIDE) (PXD037622). All other data supporting the findings in this study are included in the main article and associated files. Source data are provided with this paper.

References

1. Gawaz, M., Geisler, T. & Borst, O. Current concepts and novel targets for antiplatelet therapy. *Nat. Rev. Cardiol.* **20**, 583–599 (2023).
2. Tavassoli, P., Paterson, R. & Grant, J. *Actinobaculum schaalii*: an emerging uropathogen? *Case Rep. Urol.* **2012**, 468516 (2012).
3. Wintrobe, M. M. *Hematology, the Blossoming of a Science: a Story of Inspiration and Effort* (Lea & Febiger, 1985).
4. Machlus, K. R., Thon, J. N. & Italiano, J. E.Jr. Interpreting the developmental dance of the megakaryocyte: a review of the cellular and molecular processes mediating platelet formation. *Br. J. Haematol.* **165**, 227–236 (2014).
5. Eckly, A. et al. Biogenesis of the demarcation membrane system (DMS) in megakaryocytes. *Blood* **123**, 921–930 (2014).
6. Geue, S. et al. Pivotal role of PDK1 in megakaryocyte cytoskeletal dynamics and polarization during platelet biogenesis. *Blood* **134**, 1847–1858 (2019).
7. Bariana, T. K. et al. Sphingolipid dysregulation due to lack of functional KDSR impairs proplatelet formation causing thrombocytopenia. *Haematologica* **104**, 1036–1045 (2019).
8. Golfier, S. et al. Shaping of terminal megakaryocyte differentiation and proplatelet development by sphingosine-1-phosphate receptor S1P4. *FASEB J.* **24**, 4701–4710 (2010).
9. Zhang, L. et al. Sphingosine kinase 2 (Sphk2) regulates platelet biogenesis by providing intracellular sphingosine 1-phosphate (S1P). *Blood* **122**, 791–802 (2013).
10. Kelly, K. L. et al. De novo lipogenesis is essential for platelet production in humans. *Nat. Metab.* **2**, 1163–1178 (2020).
11. Valet, C. et al. Adipocyte fatty acid transfer supports megakaryocyte maturation. *Cell Rep.* **32**, 107875 (2020).
12. Peng, B. et al. Identification of key lipids critical for platelet activation by comprehensive analysis of the platelet lipidome. *Blood* **132**, e1–e12 (2018).
13. Manke, M.-C. et al. ANXA7 regulates platelet lipid metabolism and Ca^{2+} release in arterial thrombosis. *Circ. Res.* **129**, 494–507 (2021).
14. Molenaar, M. R. et al. LION/web: a web-based ontology enrichment tool for lipidomic data analysis. *GigaScience* **8**, giz061 (2019).
15. Peng, B. et al. LipidCreator workbench to probe the lipidomic landscape. *Nat. Commun.* **11**, 2057 (2020).
16. Han, X. Lipidomics for studying metabolism. *Nat. Rev. Endocrinol.* **12**, 668–679 (2016).
17. Borgmeyer, M. et al. Multiomics of synaptic junctions reveals altered lipid metabolism and signaling following environmental enrichment. *Cell Rep.* **37**, 109797 (2021).
18. Coman, C. et al. Simultaneous metabolite, protein, lipid extraction (SIMPLEX): a combinatorial multimolecular omics approach for systems biology. *Mol. Cell. Proteomics* **15**, 1453–1466 (2016).
19. Michel, L. et al. Targeting early stages of cardiotoxicity from anti-PD1 immune checkpoint inhibitor therapy. *Eur. Heart J.* **43**, 316–329 (2022).
20. Kuvardina, O. N. et al. RUNX1 represses the erythroid gene expression program during megakaryocytic differentiation. *Blood* **125**, 3570–3579 (2015).
21. Wang, C. Q. et al. Disruption of *Runx1* and *Runx3* leads to bone marrow failure and leukemia predisposition due to transcriptional and DNA repair defects. *Cell Rep.* **8**, 767–782 (2014).
22. Ferreira, R., Ohneda, K., Yamamoto, M. & Philipsen, S. GATA1 function, a paradigm for transcription factors in hematopoiesis. *Mol. Cell. Biol.* **25**, 1215–1227 (2005).
23. Lepage, A. et al. The $\alpha_{IIb}\beta_3$ integrin and GPIb–V–IX complex identify distinct stages in the maturation of $CD34^+$ cord blood cells to megakaryocytes. *Blood* **96**, 4169–4177 (2000).

24. Li, R. & Emsley, J. The organizing principle of the platelet glycoprotein Ib–IX–V complex. *J. Thromb. Haemost.* **11**, 605–614 (2013).
25. Nurden, A. T. & Caen, J. P. Specific roles for platelet surface glycoproteins in platelet function. *Nature* **255**, 720–722 (1975).
26. Clemetson, K. J., Pfueller, S. L., Luscher, E. F. & Jenkins, C. S. P. Isolation of the membrane glycoproteins of human blood platelets by lectin affinity chromatography. *Biochim. Biophys. Acta* **464**, 493–508 (1977).
27. Sporn, L. A., Chavin, S. I., Marder, V. J. & Wagner, D. D. Biosynthesis of von Willebrand protein by human megakaryocytes. *J. Clin. Invest.* **76**, 1102–1106 (1985).
28. Peck, B. et al. Inhibition of fatty acid desaturation is detrimental to cancer cell survival in metabolically compromised environments. *Cancer Metab.* **4**, 6 (2016).
29. Gonzalez-Covarrubias, V. et al. Lipidomics of familial longevity. *Aging Cell* **12**, 426–434 (2013).
30. Perkins, R. G. & Scott, R. E. Plasma membrane phospholipid, cholesterol and fatty acyl composition of differentiated and undifferentiated L_6 myoblasts. *Lipids* **13**, 334–337 (1978).
31. Heimerl, S. et al. Quantification of bulk lipid species in human platelets and their thrombin-induced release. *Sci. Rep.* **13**, 6154 (2023).
32. Tani, M., Sano, T., Ito, M. & Igarashi, Y. Mechanisms of sphingosine and sphingosine 1-phosphate generation in human platelets. *J. Lipid Res.* **46**, 2458–2467 (2005).
33. Niazi, H. et al. Murine platelet production is suppressed by S1P release in the hematopoietic niche, not facilitated by blood S1P sensing. *Blood Adv.* **3**, 1702–1713 (2019).
34. Haslam, R. J., Koide, H. B. & Hemmings, B. A. Pleckstrin domain homology. *Nature* **363**, 309–310 (1993).
35. Sutton, R. B., Davletov, B. A., Berghuis, A. M., Südhof, T. C. & Sprang, S. R. Structure of the first C_2 domain of synaptotagmin I: a novel Ca^{2+}/phospholipid-binding fold. *Cell* **80**, 929–938 (1995).
36. Zhang, G., Kazanietz, M. G., Blumberg, P. M. & Hurley, J. H. Crystal structure of the cys2 activator-binding domain of protein kinase Cδ in complex with phorbol ester. *Cell* **81**, 917–924 (1995).
37. Pearson, M. A., Reczek, D., Bretscher, A. & Karplus, P. A. Structure of the ERM protein moesin reveals the FERM domain fold masked by an extended actin binding tail domain. *Cell* **101**, 259–270 (2000).
38. Park, M.-J. et al. SH2 domains serve as lipid-binding modules for pTyr-signaling proteins. *Mol. Cell* **62**, 7–20 (2016).
39. Huang, K.-P. The mechanism of protein kinase C activation. *Trends Neurosci.* **12**, 425–432 (1989).
40. Murray, N. R. & Fields, A. P. Phosphatidylglycerol is a physiologic activator of nuclear protein kinase C. *J. Biol. Chem.* **273**, 11514–11520 (1998).
41. Saito, K., Scharenberg, A. M. & Kinet, J.-P. Interaction between the Btk PH domain and phosphatidylinositol-3,4,5-trisphosphate directly regulates Btk. *J. Biol. Chem.* **276**, 16201–16206 (2001).
42. Niggli, V., Andréoli, C., Roy, C. & Mangeat, P. Identification of a phosphatidylinositol-4, 5-bisphosphate-binding domain in the N-terminal region of ezrin. *FEBS Lett.* **376**, 172–176 (1995).
43. Turro, E. et al. A dominant gain-of-function mutation in universal tyrosine kinase *SRC* causes thrombocytopenia, myelofibrosis, bleeding, and bone pathologies. *Sci. Transl. Med.* **8**, 328ra30 (2016).
44. Lannutti, B. J., Shim, M.-H., Blake, N., Reems, J. A. & Drachman, J. G. Identification and activation of Src family kinases in primary megakaryocytes. *Exp. Hematol.* **31**, 1268–1274 (2003).
45. Huang, J. et al. Abivertinib inhibits megakaryocyte differentiation and platelet biogenesis. *Front. Med.* **16**, 416–428 (2022).
46. Boni, L. T. & Rando, R. R. The nature of protein kinase C activation by physically defined phospholipid vesicles and diacylglycerols. *J. Biol. Chem.* **260**, 10819–10825 (1985).
47. Newton, A. C. Lipid activation of protein kinases. *J. Lipid Res.* **50**, S266–S271 (2009).
48. Garcia, P. et al. The pleckstrin homology domain of phospholipase C-δ_1 binds with high affinity to phosphatidylinositol 4,5-bisphosphate in bilayer membranes. *Biochemistry* **34**, 16228–16234 (1995).
49. Nishizuka, Y. Intracellular signaling by hydrolysis of phospholipids and activation of protein kinase C. *Science* **258**, 607–614 (1992).
50. Bader, G. D. & Hogue, C. W. V. An automated method for finding molecular complexes in large protein interaction networks. *BMC Bioinformatics* **4**, 2 (2003).
51. Shannon, P. et al. Cytoscape: a software environment for integrated models of biomolecular interaction networks. *Genome Res.* **13**, 2498–2504 (2003).
52. Bosc, D. G. et al. Identification and characterization of CKIP-1, a novel pleckstrin homology domain-containing protein that interacts with protein kinase CK2. *J. Biol. Chem.* **275**, 14295–14306 (2000).
53. Olsten, M. E. K., Canton, D. A., Zhang, C., Walton, P. A. & Litchfield, D. W. The pleckstrin homology domain of CK2 interacting protein-1 is required for interactions and recruitment of protein kinase CK2 to the plasma membrane. *J. Biol. Chem.* **279**, 42114–42127 (2004).
54. Canton, D. A., Olsten, M. E. K., Niederstrasser, H., Cooper, J. A. & Litchfield, D. W. The role of CKIP-1 in cell morphology depends on its interaction with actin-capping protein. *J. Biol. Chem.* **281**, 36347–36359 (2006).
55. Nie, J. et al. CKIP-1: a scaffold protein and potential therapeutic target integrating multiple signaling pathways and physiological functions. *Ageing Res. Rev.* **12**, 276–281 (2013).
56. Manke, M.-C., Ahrends, R. & Borst, O. Platelet lipid metabolism in vascular thrombo-inflammation. *Pharmacol. Ther.* **237**, 108258 (2022).
57. Machlus, K. R. et al. Synthesis and dephosphorylation of MARCKS in the late stages of megakaryocyte maturation drive proplatelet formation. *Blood* **127**, 1468–1480 (2016).
58. Münzer, P. et al. CK2β regulates thrombopoiesis and Ca^{2+}-triggered platelet activation in arterial thrombosis. *Blood* **130**, 2774–2785 (2017).
59. Fan, J. et al. A novel role of CKIP-1 in promoting megakaryocytic differentiation. *Oncotarget* **8**, 30138–30150 (2017).
60. Zehentmeier, S. et al. Static and dynamic components synergize to form a stable survival niche for bone marrow plasma cells. *Eur. J. Immunol.* **44**, 2306–2317 (2014).
61. Stegner, D. et al. Thrombopoiesis is spatially regulated by the bone marrow vasculature. *Nat. Commun.* **8**, 127 (2017).
62. Rebholz, H., Zhou, M., Nairn, A. C., Greengard, P. & Flajolet, M. Selective knockout of the casein kinase 2 in D1 medium spiny neurons controls dopaminergic function. *Biol. Psychiatry* **74**, 113–121 (2013).
63. Cotte, A. K. et al. Lysophosphatidylcholine acyltransferase 2-mediated lipid droplet production supports colorectal cancer chemoresistance. *Nat. Commun.* **9**, 322 (2018).
64. Kuhajda, F. P. et al. Pharmacological glycerol-3-phosphate acyltransferase inhibition decreases food intake and adiposity and increases insulin sensitivity in diet-induced obesity. *Am. J. Physiol. Regul. Integr. Comp. Physiol.* **301**, R116–R130 (2011).
65. Heib, T., Gross, C., Müller, M.-L., Stegner, D. & Pleines, I. Isolation of murine bone marrow by centrifugation or flushing for the analysis of hematopoietic cells — a comparative study. *Platelets* **32**, 601–607 (2021).
66. Zougman, A., Selby, P. J. & Banks, R. E. Suspension trapping (STrap) sample preparation method for bottom-up proteomics analysis. *Proteomics* **14**, 1006–1000 (2014).

67. Seiser, S. et al. Octenidine-based hydrogel shows anti-inflammatory and protease-inhibitory capacities in wounded human skin. *Sci. Rep.* **11**, 32 (2021).
68. Weiss, T. et al. Schwann cell plasticity regulates neuroblastic tumor cell differentiation via epidermal growth factor-like protein 8. *Nat. Commun.* **12**, 1624 (2021).
69. Kovarik, J. J. et al. A multi-omics based anti-inflammatory immune signature characterizes long COVID-19 syndrome. *iScience* **26**, 105717 (2023).
70. Cox, J. & Mann, M. MaxQuant enables high peptide identification rates, individualized p.p.b.-range mass accuracies and proteome-wide protein quantification. *Nat. Biotechnol.* **26**, 1367–1372 (2008).
71. Cox, J. & Mann, M. 1D and 2D annotation enrichment: a statistical method integrating quantitative proteomics with complementary high-throughput data. *BMC Bioinformatics* **13**, S12 (2012).
72. Nolte, H., MacVicar, T. D., Tellkamp, F. & Krüger, M. Instant Clue: a software suite for interactive data visualization and analysis. *Sci. Rep.* **8**, 12648 (2018).
73. Peng, B. et al. A comprehensive high-resolution targeted workflow for the deep profiling of sphingolipids. *Anal. Chem.* **89**, 12480–12487 (2017).
74. Herzog, R. et al. LipidXplorer: a software for consensual cross-platform lipidomics. *PLoS ONE* **7**, e29851 (2012).
75. Herzog, R. et al. A novel informatics concept for high-throughput shotgun lipidomics based on the molecular fragmentation query language. *Genome Biol.* **12**, R8 (2011).
76. Thomas, C. P. et al. Identification and quantification of aminophospholipid molecular species on the surface of apoptotic and activated cells. *Nat. Protoc.* **9**, 51–63 (2014).
77. Rampler, E. et al. LILY-lipidome isotope labeling of yeast: in vivo synthesis of ^{13}C labeled reference lipids for quantification by mass spectrometry. *Analyst* **142**, 1891–1899 (2017).
78. Josefsson, E. C. et al. Platelet production proceeds independently of the intrinsic and extrinsic apoptosis pathways. *Nat. Commun.* **5**, 3455 (2014).
79. Schneider, C. A., Rasband, W. S. & Eliceiri, K. W. NIH Image to ImageJ: 25 years of image analysis. *Nat. Methods* **9**, 671–675 (2012).

Acknowledgements

This study was funded by the Deutsche Forschungsgemeinschaft (DFG, German Research Foundation), project numbers 374031971 – CRC240, BO3786/3-1 and BO3786/7-1, 453989101 – CRC1525 (O.B.), and the Austrian Science Fund, FWF DMP I6303. The funders had no role in study design, data collection and analysis, decision to publish, or preparation of the manuscript. The authors received support from the University of Vienna through seed funding and funding derived from the Vienna Doctoral School in Chemistry (DoSChem) at the Faculty of Chemistry, University of Vienna (R.A.), as well as from the DigiOmics4Austria: BMBWF Ausschreibung "(Digitale) Forschungsinfrastrukturen" (R.A.). We further thank V. O'Donnell (Systems Immunity Research Institute, School of Medicine, Cardiff University) for providing PS surface labeling protocols and D. Eißler (DFG Heisenberg Group Cardiovascular Thromboinflammation and Translational Thrombocardiology, University of Tübingen, and Department of Cardiology and Angiology, University of Tübingen) for excellent technical assistance.

Author contributions

O.B. and R.A. developed the concept. B.d.J., F.K., P.M., O.B. and R.A. designed, conducted and analyzed the experiments. V.G., M.F., K.M., N.N.T., M.-C.M., M.Z. and M.S. conducted experiments. T.H., D.K., A.B., C.G., N.H., D.H., A.A., M.G., D.S. and H.S. analyzed data. C.C. reviewed the methodological aspect with R.A. O.B. and R.A. supervised and coordinated the project. All authors wrote and revised the manuscript.

Competing interests

The authors declare no competing financial interests.

Additional information

Extended data is available for this paper at https://doi.org/10.1038/s44161-023-00325-8.

Supplementary information The online version contains supplementary material available at https://doi.org/10.1038/s44161-023-00325-8.

Correspondence and requests for materials should be addressed to Oliver Borst or Robert Ahrends.

Peer review information *Nature Cardiovascular Research* thanks John Hwa, Matthew A Mitsche and Angel Garcia Alonso for their contribution to the peer review of this work.

Reprints and permissions information is available at www.nature.com/reprints.

Publisher's note Springer Nature remains neutral with regard to jurisdictional claims in published maps and institutional affiliations.

Open Access This article is licensed under a Creative Commons Attribution 4.0 International License, which permits use, sharing, adaptation, distribution and reproduction in any medium or format, as long as you give appropriate credit to the original author(s) and the source, provide a link to the Creative Commons license, and indicate if changes were made. The images or other third party material in this article are included in the article's Creative Commons license, unless indicated otherwise in a credit line to the material. If material is not included in the article's Creative Commons license and your intended use is not permitted by statutory regulation or exceeds the permitted use, you will need to obtain permission directly from the copyright holder. To view a copy of this license, visit http://creativecommons.org/licenses/by/4.0/.

© The Author(s) 2023, corrected publication 2023

https://doi.org/10.1038/s44161-023-00325-8

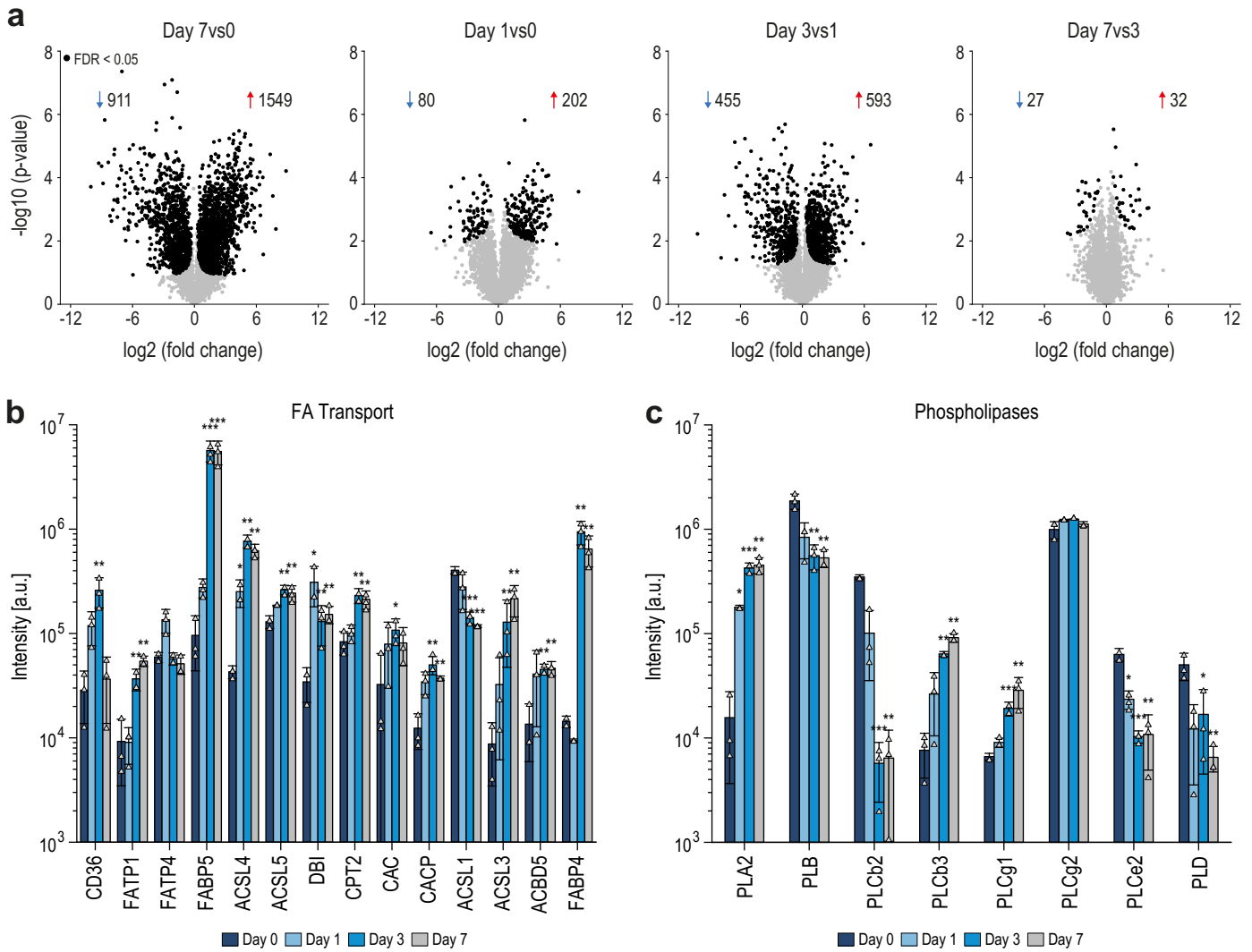

Extended Data Fig. 1 | See next page for caption.

https://doi.org/10.1038/s44161-023-00325-8

Extended Data Fig. 1 | Protein regulation highlighting key proteins involved in lipid metabolism. Related to Fig. 1. a, Volcano plots of -$\log_{10}$ p-values over $\log_2$ fold changes of all identified proteins on day 0, 1, 3 and 7 of MK maturation. P-values were corrected using the Benjamini-Hochberg correction with an FDR cut-off of 0.05. **b,c**, Proteins of fatty acid transport pathways (**b**) as well as identified phospholipases (**c**) are depicted. A two-sided t-test was used for statistical analysis. Benjamini-Hochberg correction was applied to p-values using an FDR cut-off < 0.05 (*P ≤ 0.05, **P ≤ 0.01, ***P ≤ 0.001). **d**, Network highlighting proteins involved in lipid metabolism. Edges are correlations of r ≥ 0.85. Nodes represent proteins and the node color the associated lipid category (left). The network on the right is color-coded based on the $\log_2$ fold change of proteins regulated from day 0 to day 7. Pure red indicates an FC ≥ 2 and pure blue an FC ≤ -2. Data are combined from 3 independent biological experiments and mean values are shown. Error bars represent standard deviations.

https://doi.org/10.1038/s44161-023-00325-8

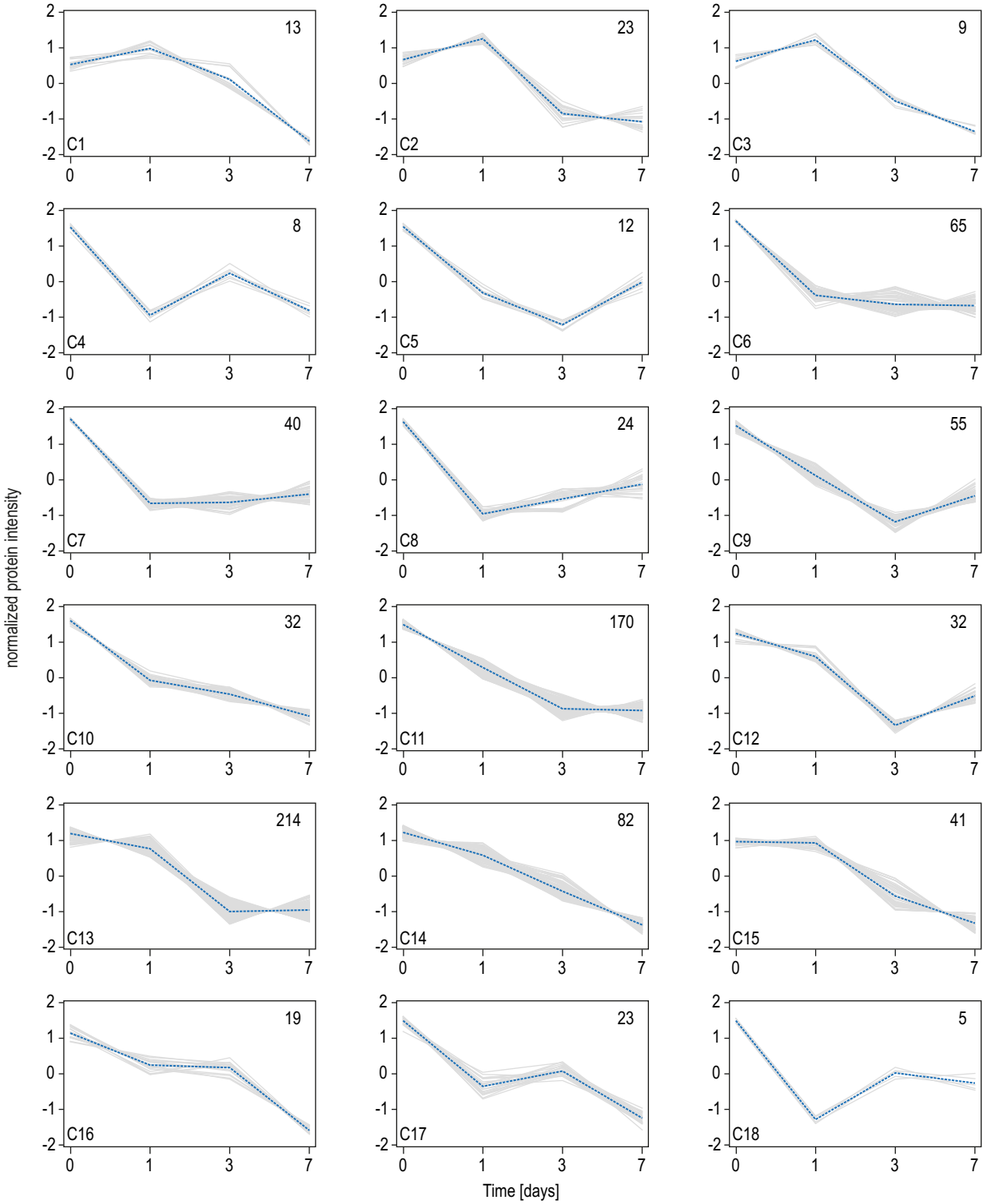

Extended Data Fig. 2 | Fuzzy c-means clustering of down-regulated proteins during MK maturation. Related to Fig. 1. Protein cluster (C1-C18) showing overall downregulation. Number of proteins and their median are denoted in individual plots as well as the associated cluster (C1-C18). The assignment of proteins to clusters can be found in the Source Data. Threshold = 85.

https://doi.org/10.1038/s44161-023-00325-8

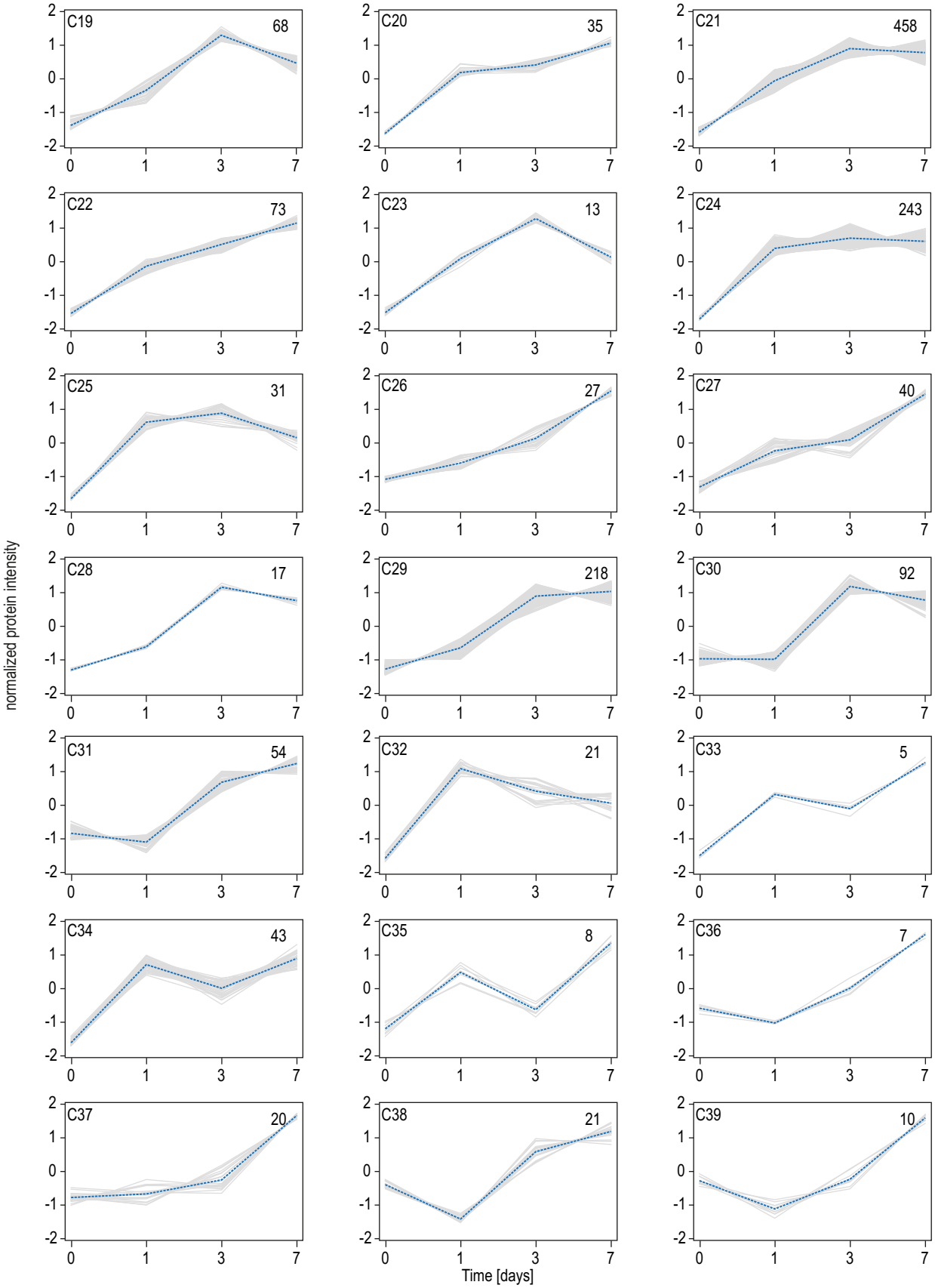

Extended Data Fig. 3 | Fuzzy c-means clustering of up-regulated proteins during MK maturation. Related to Fig. 1. Protein cluster (C19-C39) showing overall upregulation. Number of proteins and their median are denoted in individual plots as well as the associated cluster (C19-C39). The assignment of proteins to clusters can be found in the Source Data. Threshold = 85.

https://doi.org/10.1038/s44161-023-00325-8

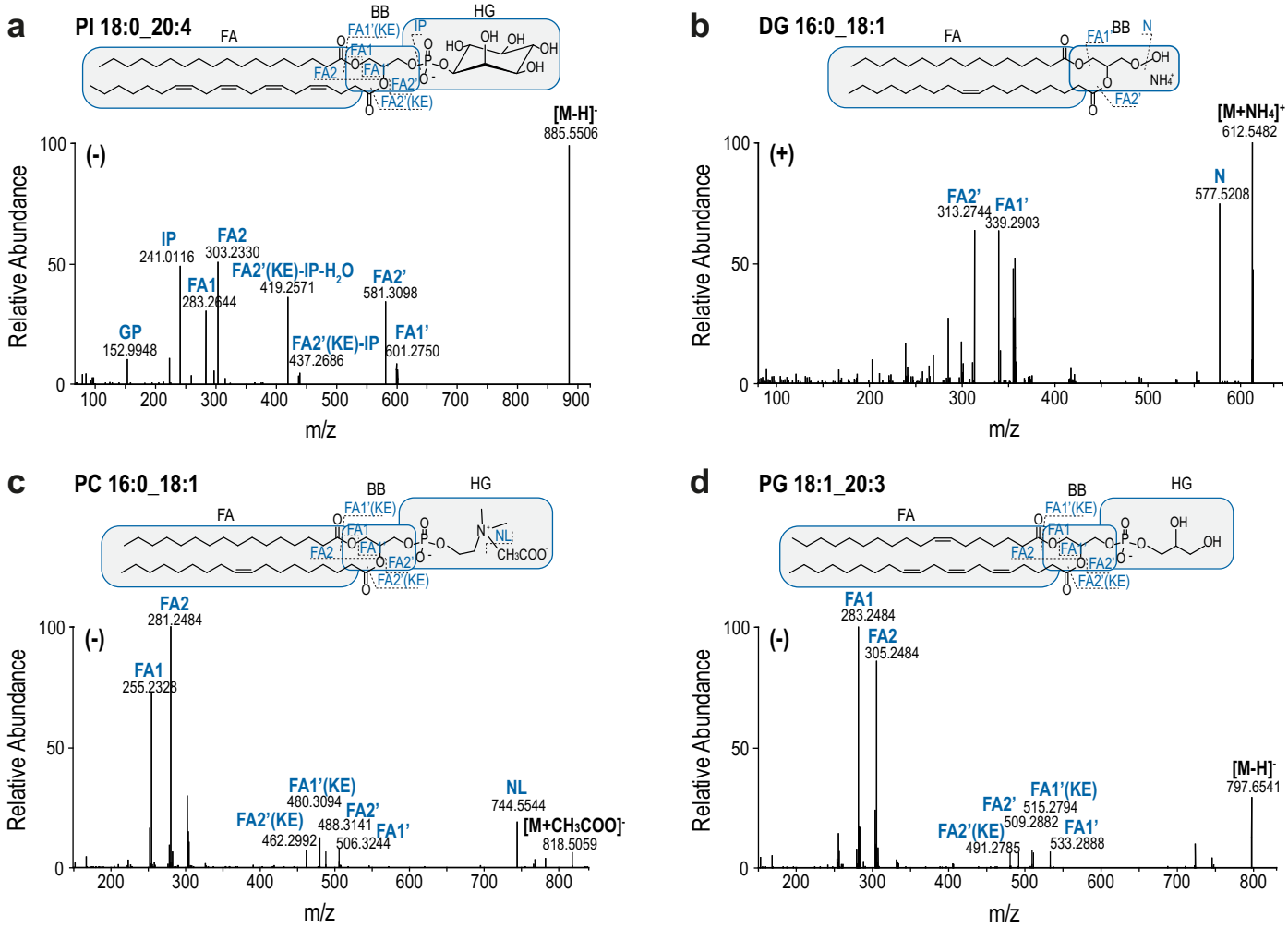

Extended Data Fig. 4 | Structural elucidation at the FA level of lipids in the main lipid categories. Related to Fig. 2. a-d, Molecular structural analysis of lipids identified with shotgun lipidomics at the MS2 level. The MS2 spectra shown in each panel are used as structural assessment by customized MFQL search files using the LipidXplorer search engine. Potential fragmentation patterns are shown above each panel. Annotated fragments are denoted in the chemical structure of the individual species. For lipid identification, FAs and loss of FAs as well as class-specific headgroups or neutral losses were used. Quantification of lipid species on the molecular species level is based on FA intensities.

https://doi.org/10.1038/s44161-023-00325-8

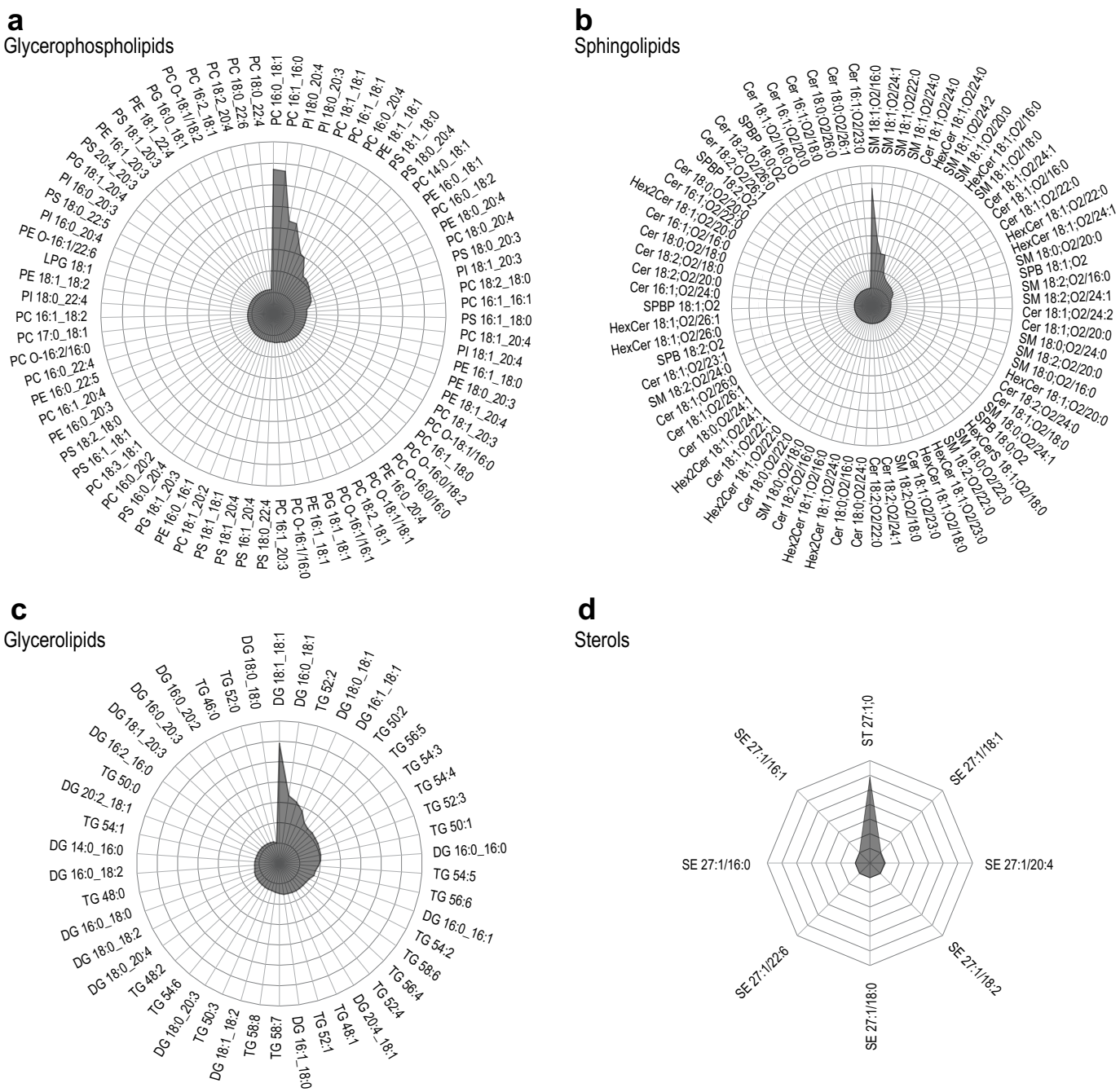

Extended Data Fig. 5 | Quantitative elucidation at the FA level of lipids in the main lipid categories. Related to Fig. 2. a-d, Radar charts displaying the relative intensity of lipid species of mature MKs organized according to their lipid category, including GP, SP, GL, and STs. GPs and GLs were analyzed with shotgun lipidomics while SPs and STs were analyzed with targeted lipidomics.

https://doi.org/10.1038/s44161-023-00325-8

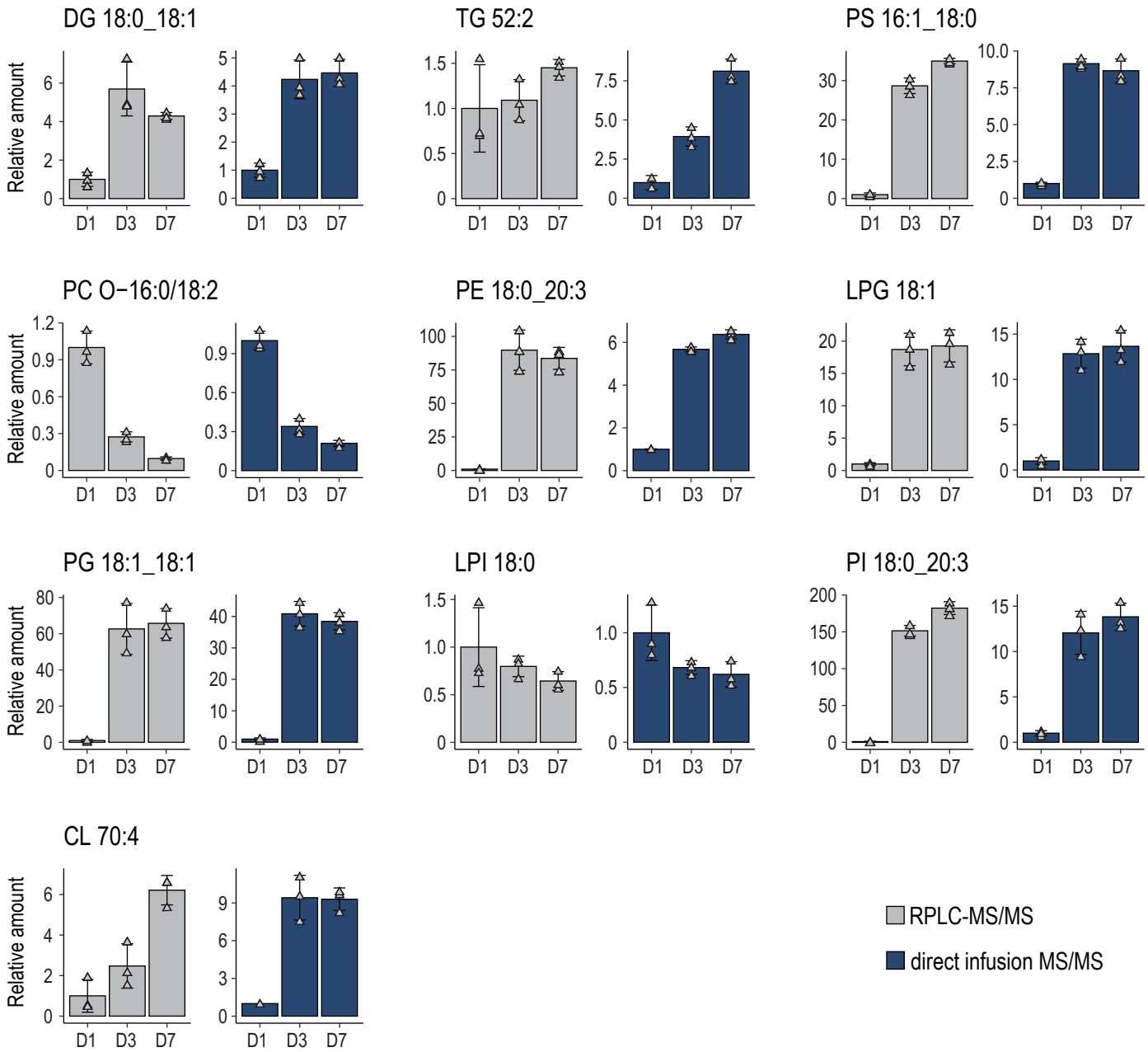

Extended Data Fig. 6 | Validation of shotgun lipidomics data by targeted RPLC-MS/MS. Related to Fig. 4. Trends of selected class representative lipid species were confirmed by targeted reverse-phase LC-MS/MS. Shown in blue are data obtained from shotgun measurements, shown in grey are results from LC experiments. For better comparison of observed lipid trends, lipid quantities are shown as relative amount compared to day 1. All data show the mean of 3 biological replicates. One biological replicate was comprised of 5 individual animals. Error bars represent standard deviations.

https://doi.org/10.1038/s44161-023-00325-8

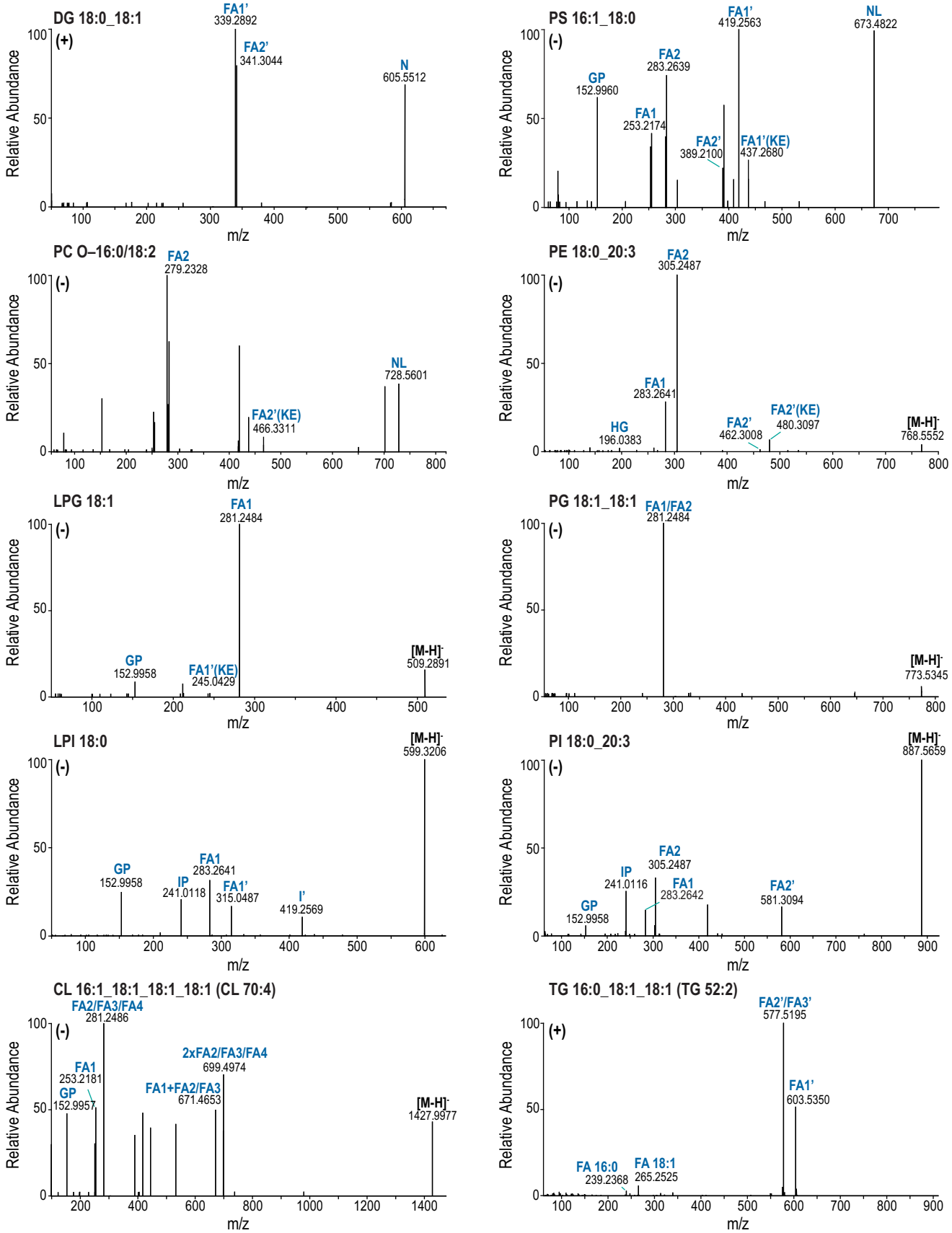

Extended Data Fig. 7 | See next page for caption.

https://doi.org/10.1038/s44161-023-00325-8

Extended Data Fig. 7 | MS2 spectra for the structural elucidation of representative lipid species. Related to Fig. 4. All MS2 spectra were acquired using a collision energy of 21 % in positive ion mode and 24 % in negative ion mode at R m/z_{200} of 30000. GP (glycerol phosphate backbone), FA (fatty acyl), HG (class specific head group fragment), IP (inositol phosphate), I (inositol) and NL (neutral loss of class specific headgroup), indicate structure specific fragments. Scan polarity is indicated on the upper left side of each panel. The fragments annotated were used for lipid identification. Quantification of lipid species on the molecular species level is based on FA intensities. CL and TG were quantified on MS1 level based on precursor intensities.

https://doi.org/10.1038/s44161-023-00325-8

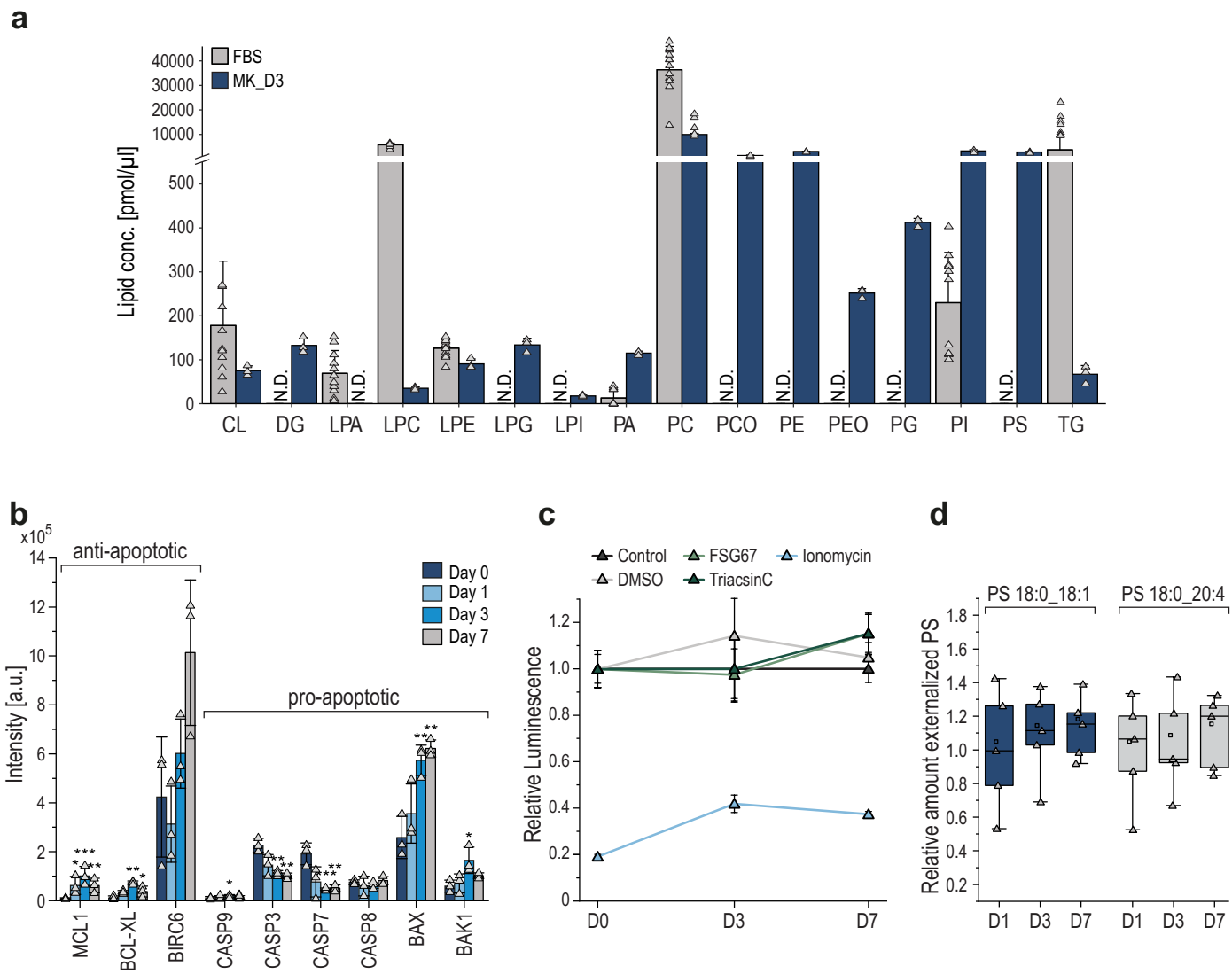

Extended Data Fig. 8 | Exclusion of media lipid composition and apoptosis as confounding factors for observed lipidomic changes in MKs. Related to Fig. 4. **a**, Distribution of main lipid classes from mature MKs (day 3, n = 3) as well as FBS (n = 11) used for cell culture supplementation. Lipid quantities were normalized to volume. **b**, Proteomic analysis of pro- and anti-apoptotic markers in MKs. A two-sided t-test was used for statistical analysis. Benjamini-Hochberg correction was applied to p-values using an FDR cut-off < 0.05 (*P ≤ 0.05, **P ≤ 0.01, ***P ≤ 0.001). **c**, ATP cell vitality assay showing MKs treated with inhibitors. Ionomycin was used as positive control for apoptotic cells. The measured luminescence was normalized to the control for each day to display changes relative to the control baseline (dark grey). **d**, PS externalization during megakaryopoiesis. The two most abundant PS species were monitored. Externalization was calculated by dividing the amount of biotinylated PS on the cell surface by the total biotinylated PS, as described in the methods. Lipid quantities of day 1 were used as reference and set to 1. All other days were calculated as ratios relative to day 1 (n = 5). All data show the mean of at least 3 biological replicates. One biological replicate was comprised of 5 individual animals. In **a**-**b**, error bars represent standard deviations. In **d**, boxplot whiskers represent the minimum and maximum. The boundaries of the box represent the 25th and 75th percentile. Middle black lines represent the mean and black squares indicate the median.

https://doi.org/10.1038/s44161-023-00325-8

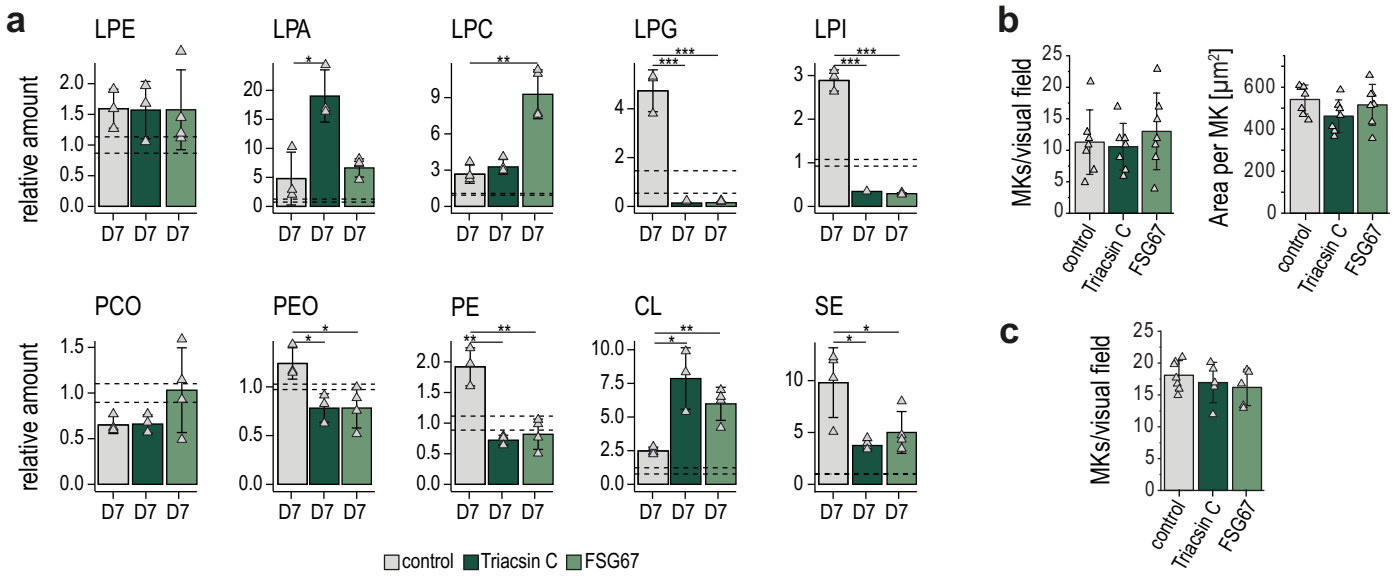

Extended Data Fig. 9 | Analysis of the megakaryocytes upon inhibition of phospholipid biosynthesis. Related to Fig. 5. a, Lipidome analysis showing the relative quantities (mean ± SD, n = 4) per lipid class of control and inhibitor treated MKs on day 7. Non-treated day 0 MKs were used as baseline control and lipid quantities were set to 1 and the standard deviation is depicted as dotted lines. Changes for all lipid classes were calculated as ratios relative to control day 0. A two-sided t-test was used for statistical analysis. All days were tested against day 7 control (*P ≤ 0.05, **P ≤ 0.01, ***P ≤ 0.001). **b**, Arithmetic means ± SD (n = 5-7) of MKs of Triacsin C, FSG67 or vehicle treated mice per visual field of *in vivo* imaging in the BM vasculature of the frontoparietal skull of mice. **c**, Arithmetic mean ± SD (n = 5-7) of MKs and MK area of Triacsin C, FSG67 or vehicle treated mice per visual field in immunostained BM sections.

https://doi.org/10.1038/s44161-023-00325-8

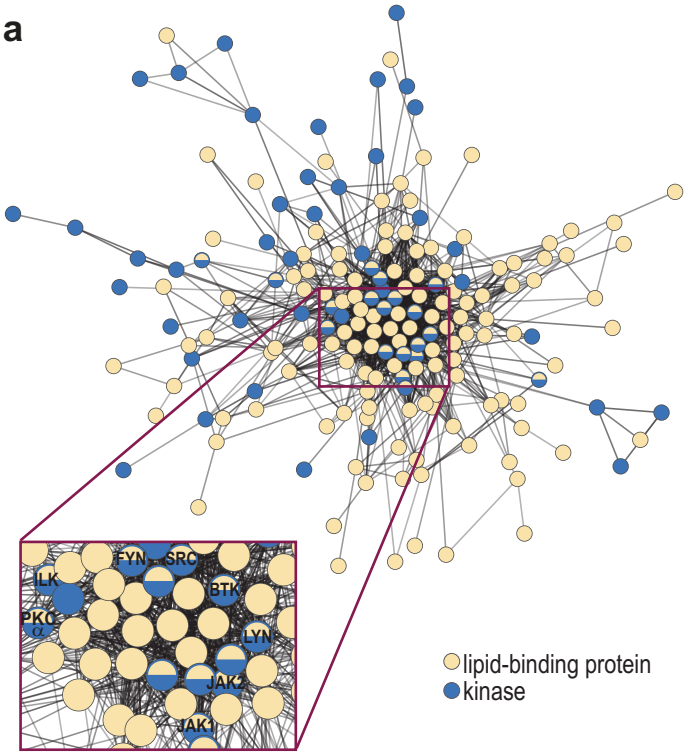

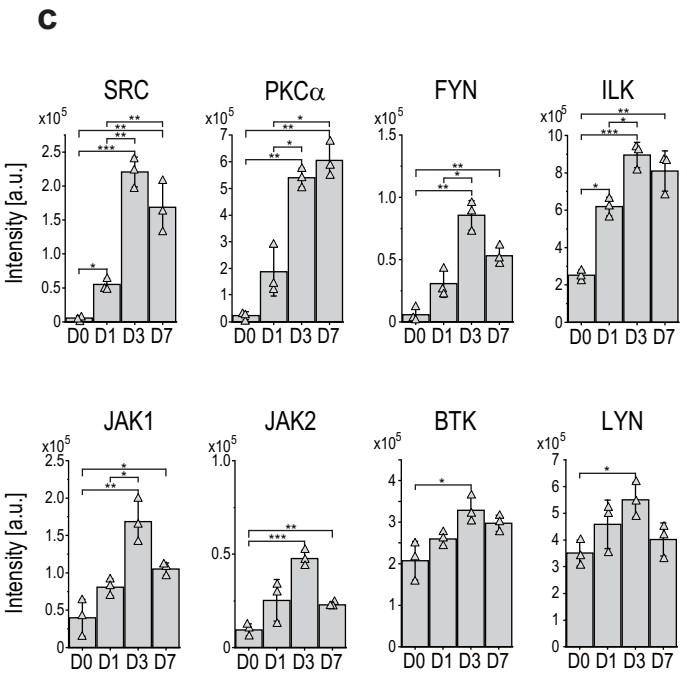

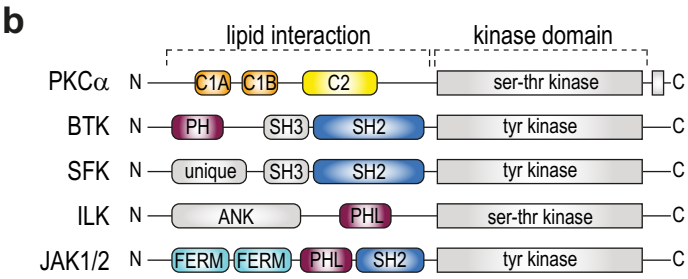

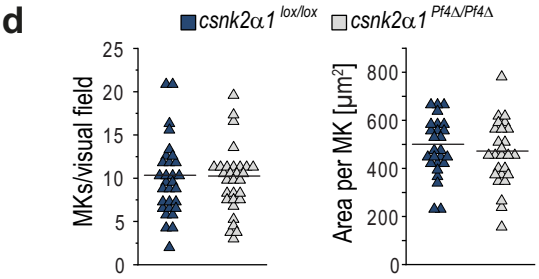

Extended Data Fig. 10 | Lipid-dependent kinases in MKs involved in megakaryopoiesis and proplatelet formation. Related to Fig. 6. **a**, Network showing significantly regulated kinases (blue) and lipid-binding proteins (yellow). Edges are correlations with a minimum interaction confidence score 0.5. Nodes are proteins. **b**, Domain composition of depicted kinases. Membrane-targeting modules are the C1 (orange), C2 (yellow), pleckstrin homology (PH) or PH-like (purple), and FERM (light blue) domains. Additional interaction domains like Src-homology (SH) domains are shown in dark blue. Kinase domains are shown in gray. Note, the schematic representation is not reproduced in the correct domain proportions and does not reflect the actual protein size. **c**, Regulation of kinases with a lipid binding domain (mean ± SD, n = 3). A two-sided t-test was used for statistical analysis. Benjamini Hochberg correction was applied to p-values using an FDR cut-off of 0.05 (*P ≤ 0.05, **P ≤ 0.01, ***P ≤ 0.001). **d**, Arithmetic means of MKs and MK area of *csnk2α1*$^{lox/lox}$ and *csnk2α1*$^{Pf4Δ/Pf4Δ}$ mice per visual field (n = 30) in immunostained BM sections.

nature research

Corresponding author(s): Oliver Borst & Robert Ahrends

Last updated by author(s): Jul 26, 2023

Reporting Summary

Nature Research wishes to improve the reproducibility of the work that we publish. This form provides structure for consistency and transparency in reporting. For further information on Nature Research policies, see Authors & Referees and the Editorial Policy Checklist.

Statistics

For all statistical analyses, confirm that the following items are present in the figure legend, table legend, main text, or Methods section.

n/a	Confirmed	
☐	☒	The exact sample size (*n*) for each experimental group/condition, given as a discrete number and unit of measurement
☐	☒	A statement on whether measurements were taken from distinct samples or whether the same sample was measured repeatedly
☐	☒	The statistical test(s) used AND whether they are one- or two-sided *Only common tests should be described solely by name; describe more complex techniques in the Methods section.*
☒	☐	A description of all covariates tested
☐	☒	A description of any assumptions or corrections, such as tests of normality and adjustment for multiple comparisons
☐	☒	A full description of the statistical parameters including central tendency (e.g. means) or other basic estimates (e.g. regression coefficient) AND variation (e.g. standard deviation) or associated estimates of uncertainty (e.g. confidence intervals)
☐	☒	For null hypothesis testing, the test statistic (e.g. *F*, *t*, *r*) with confidence intervals, effect sizes, degrees of freedom and *P* value noted *Give P values as exact values whenever suitable.*
☒	☐	For Bayesian analysis, information on the choice of priors and Markov chain Monte Carlo settings
☒	☐	For hierarchical and complex designs, identification of the appropriate level for tests and full reporting of outcomes
☒	☐	Estimates of effect sizes (e.g. Cohen's *d*, Pearson's *r*), indicating how they were calculated

Our web collection on statistics for biologists contains articles on many of the points above.

Software and code

Policy information about availability of computer code

Data collection	No data was collected.
Data analysis	LipidCreator (version 1.2.0) was used for creating transition lists for targeted lipidomics analysis. LipidXplorer (version 1.2.8.1) was used for lipid identification of direct-infusion MS/MS data. MSConvert (version 3.0.20186-dd907d757) was used for centroiding shotgun lipidomic data. Skyline (version 21.1.0.146) was used to search and quantify the targeted lipids. Analyst (version 1.7.2) was used to acquire targeted lipidomic data. Cytoscape (version 3.9.1) was used to generate protein networks and identify protein clusters. MaxQuant (version 1.6.17.0) was for label-free protein quantification. Perseus (version 1.6.14.0) was used for post-processing of MaxQuant searches and statistical testing. InstantClue (version 0.10.10) was used for visualization of proteomic data (volcano plots). OriginPro (version 2021) was used for statistical analysis and data visualization. Rstudio (version 1.4.1106) was used for data visualization. NIS Elements Imaging software (version 5.21.00) was used for examination of proplatelet formation. ZEN Blue (version 2.3) was used for the analysis of immunofluorescence microscopy images. LAS X (version 5.1.0) was used for the analysis of femora cryosections. FlowJo software (version 10.8.0) was used for analysis of flow cytometry data. ImageJ software (NIH) (version 1.53a) was used for immunoblot analysis and generation of movies.

For manuscripts utilizing custom algorithms or software that are central to the research but not yet described in published literature, software must be made available to editors/reviewers. We strongly encourage code deposition in a community repository (e.g. GitHub). See the Nature Research guidelines for submitting code & software for further information.

Data

Policy information about availability of data

All manuscripts must include a data availability statement. This statement should provide the following information, where applicable:

- Accession codes, unique identifiers, or web links for publicly available datasets
- A list of figures that have associated raw data
- A description of any restrictions on data availability

Lipidomics data have been deposited at Zenodo (DOI:10.5281/zenodo.8186280) for immediate access. After publication, data will be further accessible at Metabolights (MTBLS6082, MTBLS6083, MTBLS6084). Proteomics data have been deposited at PRIDE (PXD037622).
Protein sequences were obtained from the publicly available SwissProt database mus musculus (v220621 with 17519 entries).
All other data supporting the findings in this study are included in the main article and associated files. Source data are provided with the manuscript

Field-specific reporting

Please select the one below that is the best fit for your research. If you are not sure, read the appropriate sections before making your selection.

☒ Life sciences ☐ Behavioural & social sciences ☐ Ecological, evolutionary & environmental sciences

For a reference copy of the document with all sections, see nature.com/documents/nr-reporting-summary-flat.pdf

Life sciences study design

All studies must disclose on these points even when the disclosure is negative.

Sample size	Sample size was determined taking into account the 3 R´s for animal experimentation and the expected experimental variability. At least 3 biological replicates were used for lipidomics or proteomic analysis of MKs. For biochemistry approaches sample sizes were at least n=5 unless stated otherwise. Sample sizes were chosen on the basis of standard power calculations (with a=0,05 and power of 0.8) performed for similar experiments.
Data exclusions	No data was excluded from the analysis.
Replication	For lipidomics analysis, the full set of samples was measured at least twice, to verify observed trends. Proteomic data was acquired only once from three biological replicates in technical duplicates. For biochemistry approaches experimental findings were replicated at least five times independently with different animals to guarantee maximum reproducibility, described in detail in each figure legend. In addition, the main conclusions are supported by several different experiments using different techniques (Lipidomics, proteomics and functional phenotypic analysis in vitro and in vivo). All attempts at experimental replication were successful.
Randomization	Animals were taken from different litters and cages, and placed randomly based on the experiments. For lipidomics analysis of MK, groups and samples were allocated in random order to eliminate time dependent effects on sample preparation. For investigation regarding csnk2a1 mice, animals were selected for a posteriori analysis based on their genotype.
Blinding	The investigators were blinded during the experiments and the result analysis.

Reporting for specific materials, systems and methods

We require information from authors about some types of materials, experimental systems and methods used in many studies. Here, indicate whether each material, system or method listed is relevant to your study. If you are not sure if a list item applies to your research, read the appropriate section before selecting a response.

Materials & experimental systems

n/a	Involved in the study
☐	☒ Antibodies
☒	☐ Eukaryotic cell lines
☒	☐ Palaeontology
☐	☒ Animals and other organisms
☒	☐ Human research participants
☒	☐ Clinical data

Methods

n/a	Involved in the study
☒	☐ ChIP-seq
☐	☒ Flow cytometry
☒	☐ MRI-based neuroimaging

Antibodies

Antibodies used	Details of all antibodies are provided within the Methods. Rabbit anti-a-tubulin (Thermo Fisher Scientific, PA5-19489), 1:400, polyclonal rat anti-CD42b, monoclonal (Emfret, M042-1), 1:100, Xia.G7

rat FITC anti-mouse CD41 (Biolegend, 133904), 1:100, MWReg30
rabbit anti-CSNK2A1 (Abcam, ab76040), 1:1000, EP1963Y
mouse anti-CKIP1 (Santa Cruz, sc-376355), 1:200, A-12
mouse anti-GAPDH (Thermo Fisher Scientific, MA5-15738), 1:1000, GA1R
goat anti-rabbit secondary antibody (Life Technologies, A21069), 1:300, polyclonal
goat anti-rat secondary antibody (Life Technologies, A11006), 1:300, polyclonal
donkey anti-mouse secondary antibody (LI-COR, 926-32212), 1:15000, polyclonal
Alexa594-conjugated anti-CD105 antibody (BioLegend, 120418), 1:300, MJ7/18
Alexa546-conjugated anti-CD105 (self-generated, clone MJ7/1860), 0.6 µg/g body weight
anti-CD42a (GPIX) Alexa Fluor 488 derivative (self-generated, p0p661), 0.8 µg/g body weight

Validation

Antibodies were previously validated for immunofluorescence of mouse tissue either in the laboratory of ourselves or commercial supplier. For specificity statements see manufacturers websites.
Rabbit anti-a-tubulin: https://www.thermofisher.com/antibody/product/alpha-Tubulin-Antibody-Polyclonal/PA5-19489
rat anti-CD42b: https://www.emfret.com/fileadmin/user_upload/Datasheets/M042-1_XiaG7.pdf
rat FITC anti-mouse CD41: https://www.biolegend.com/en-us/products/fitc-anti-mouse-cd41-antibody-5896
rabbit anti-CSNK2A1: https://www.abcam.com/products/primary-antibodies/csnk2a1-antibody-ep1963y-ab76040.html
mouse anti-CKIP1: https://datasheets.scbt.com/sc-376355.pdf
mouse anti-GAPDH: https://www.thermofisher.com/antibody/product/GAPDH-Loading-Control-Antibody-clone-GA1R-Monoclonal/MA5-15738
goat anti-rabbit secondary antibody: https://www.thermofisher.com/antibody/product/Goat-anti-Rabbit-IgG-H-L-Secondary-Antibody-Polyclonal/A-21069
goat anti-rat secondary antibody: https://www.thermofisher.com/antibody/product/Goat-anti-Rat-IgG-H-L-Cross-Adsorbed-Secondary-Antibody-Polyclonal/A-11006
donkey anti-mouse secondary antibody: https://www.licor.com/bio/reagents/irdye-800cw-donkey-anti-mouse-igg-secondary-antibody
Alexa594-conjugated anti-CD105 antibody: https://www.biolegend.com/en-us/products/alexa-fluor-594-anti-mouse-cd105-antibody-15440
Alexa546-conjugated anti-CD105: Zehentmeier, S., et al., Eur J Immunol., 2014, PMID: 24777940
anti-CD42a (GPIX) Alexa Fluor 488 derivative: Nieswandt, B., et al., Blood, 2000, PMID: 11001906

Animals and other organisms

Policy information about studies involving animals; ARRIVE guidelines recommended for reporting animal research

Laboratory animals

For normal MK differentiation experiments, MKs from bone marrow of 10-14 weeks old, male C57BL/6J mice (Jackson Laboratory) were used.
Csnk2a1lox/lox mice were generated elsewhere (PMID: 23290496). For megakaryocyte (MK)/platelet-specific deletion of CK2α, csnk2a1lox/lox mice were crossed with Pf4-Cre transgenic mice (Jackson Laboratory, #008535) and male mice were studied at the age of 12-14 weeks.
For in vivo treatment studies, C57BL6/J male mice with approximately 20 g body weight were used.
Mouse housing underlies a 12 hours light/12 hours dark cycle. Temperatures of 65-75°F (~18-23°C) with 40-60% humidity are provided. Water and food are accessible ad libitum.

Wild animals

The study did not involve wild animals.

Field-collected samples

The study did not involve samples collected from the field.

Ethics oversight

All animal experiments were performed according to the Directive 2010/63/EU of the European Parliament on the protection of animals used for scientific purposes and were approved by local authorities (Regierungspräsidium Tübingen) following the ARRIVE guidelines.

Note that full information on the approval of the study protocol must also be provided in the manuscript.

Flow Cytometry

Plots

Confirm that:

☒ The axis labels state the marker and fluorochrome used (e.g. CD4-FITC).

☒ The axis scales are clearly visible. Include numbers along axes only for bottom left plot of group (a 'group' is an analysis of identical markers).

☒ All plots are contour plots with outliers or pseudocolor plots.

☒ A numerical value for number of cells or percentage (with statistics) is provided.

Methodology

Sample preparation

The bone marrow of femora bones from mice was flushed and homogenized. Cells were cultivated in 10 cm cell culture dishes containing DMEM (supplemented with 1 % penicillin / streptomycin and 10 % FBS) and differentiation was initiated by adding (1%) recombinant TPO. After 5-day cultivation, the cell suspension was carefully pipetted on a two-phase BSA gradient (bottom: 1.5 ml 3 % BSA in PBS, top: 1.5 ml 1.5 % BSA in PBS) to separate cells by weight. After 40 minutes, the supernatant was removed

	and the cell pellet was washed 3 times with 500 µl PBS. Non-specific BM binding was blocked by incubation with 0.02 mg/ml FcR Blocking Reagent. Afterwards, MKs were stained using FITC-conjugated anti-CD41 antibody and the cells were subsequently washed once with 2 mM EDTA in PBS. Cells then were washed with PBS (5 min at 300 xg) and fixed in PBS containing 1% PFA/0.1% EDTA. Fixed cells were washed with PBS (10 min at 300 xg) and permeabilized in PBS containing 0.1% TritonX-100. Finally, DNA was stained using 50 µg/ml propidium iodide staining solution containing 100 µg/ml RNaseA and 2 mM EDTA in PBS. Analysis was performed by flow cytometry (BD FACSCalibur, Biosciences) and FlowJo software (Tree Star Inc).
Instrument	BD FACSCalibur, Biosciences
Software	FlowJo software 10.8.0 (Tree Star Inc)
Cell population abundance	Megakaryocyte abundance was assessed using CD41 and ranged between 70-90%.
Gating strategy	To determine the ploidy distribution of megakaryocytes, cells were identified by FSC and SSC values. CD41+ cells were considered MK's and plotted against propidium iodide signal. Quantification was performed by histogram analysis.

☒ Tick this box to confirm that a figure exemplifying the gating strategy is provided in the Supplementary Information.